# Enhanced joint hybrid deep neural network explainable artificial intelligence model for 1-hr ahead solar ultraviolet index prediction

Salvin S. Prasad [a], Ravinesh C. Deo [a,*], Sancho Salcedo-Sanz [a,c], Nathan J. Downs [b], David Casillas-Pérez [d], Alfio V. Parisi [b]

[a] School of Mathematics, Physics and Computing, University of Southern Queensland, Springfield, QLD 4300, Australia
[b] School of Mathematics, Physics and Computing, University of Southern Queensland, Toowoomba, QLD 4350, Australia
[c] Department of Signal Processing and Communications, Universidad de Alcalá, Alcalá de Henares, 28805, Madrid, Spain
[d] Department of Signal Processing and Communications, Universidad Rey Juan Carlos, Fuenlabrada, 28942, Madrid, Spain

## ARTICLE INFO

## ABSTRACT

*Background and Objective:* Exposure to solar ultraviolet (UV) radiation can cause malignant keratinocyte cancer and eye disease. Developing a user-friendly, portable, real-time solar UV alert system especially or wearable electronic mobile devices can help reduce the exposure to UV as a key measure for personal and occupational management of the UV risks. This research aims to design artificial intelligence-inspired early warning tool tailored for short-term forecasting of UV index (*UVI*) integrating satellite-derived and ground-based predictors for Australian hotspots receiving high UV exposures. The study further improves the trustworthiness of the newly designed tool using an explainable artificial intelligence approach.

*Methods:* An enhanced joint hybrid explainable deep neural network model (called EJH-X-DNN) is constructed involving two phases of feature selection and hyperparameter tuning using Bayesian optimization. A comprehensive assessment of EJH-X- DNN is conducted with six other competing benchmarked models. The proposed model is explained locally and globally using robust model-agnostic explainable artificial intelligence frameworks such as Local Interpretable Model-Agnostic Explanations (LIME), Shapley additive explanations (SHAP), and permutation feature importance (PFI).

*Results:* The newly proposed model outperformed all benchmarked models for forecasting hourly horizons *UVI*, with correlation coefficients of 0.900, 0.960, 0.897, and 0.913, respectively, for Darwin, Alice Springs, Townsville, and Emerald hotspots. According to the combined local and global explainable model outcomes, the site-based results indicate that antecedent lagged memory of *UVI* and solar zenith angle are influential features. Predictions made by EJH-X-DNN model are strongly influenced by factors such as ozone effect, cloud conditions, and precipitation.

*Conclusion:* With its superiority and skillful interpretation, the *UVI* prediction system reaffirms its benefits for providing real-time UV alerts to mitigate risks of skin and eye health complications, reducing healthcare costs and contributing to outdoor exposure policy.

## 1. Introduction

Exposure to solar ultraviolet (UV) radiation (290-400 nm) poses both beneficial and harmful effects on people, as well as terrestrial animal and plant life. In terms of benefits, exposure to UV radiation enables the human body to produce a sufficient amount of vitamin D that helps strengthen muscles, bones and the overall immune system [1]. The ability of UV radiation to inactivate potentially harmful micro-organisms (such as protozoa) has led to its application as a disinfectant in the water and food industry [2]. Recently, UV light was increasingly utilized as a significant disinfectant for coronavirus-contaminated surfaces during the COVID-19 pandemic [3]. Contrary to the benefits, elevated exposure to UV light radiation causes temporary or irreversible damage to the process of photosynthesis in plants [4]. Above all, the most pressing

concern for the health sector is the detrimental effects of erythemally-effective UV irradiance at the short end of the spectrum (290 to 315 nm) that poses high exposure risks for human skin and eyes [5,6]. Prolonged UV exposure may result in skin-based malignant keratinocyte cancers and eye diseases that include cataracts and pterygium [7].

UV radiation-induced skin cancers have led to an increased mortality rate in most temperate countries. In 2018, there was a significant mortality of 126,000 for skin cancer on a global basis, which imposes a profound economic burden on healthcare services [8]. Having a high ambient UV irradiance and prevalence of fair skin types in the Australian and New Zealand population, the two countries recorded the highest incidence of melanoma and keratinocyte carcinoma on a global basis in 2021 [9]. In Australia, such skin-related public health problems are more severe and they impose a huge burden on the Australian health sector with an annual estimated expenditure of $1.7 billion (AUD) on skin cancer treatment [10].

In order to develop engineering-based solutions for wearable electronics and other personal protection tools that can implement sun protection and mitigate the impacts of sun-exposure-related skin and eye health risks, the World Health Organization (WHO), International Commission on Non-Ionizing Radiation Protection (ICNIRP), World Meteorological Organization (WMO) and United Nations Environment Programme (UNEP) have developed the global solar UV index (*UVI*). This is a numeric-scale indicator of the public health risk of UV, ranging from 0 to 11$^+$ [11]. With a high *UVI*, the associated UV exposure severity and potential damage to the skin and eye is expected to rise. Preventative interventions with innovative decision support tools capable of providing sun exposure information to individuals can help mitigate the detrimental effects of UV exposure, as well as reduce healthcare costs. For some decades, ground-based [5] and satellite-based [6] instrumentations have been commonly employed to estimate the incoming solar UV irradiance. Though the two approaches can deliver accurate sun-exposure information, the major drawback of their practical utility is the high costs of installation, maintenance and operation [12].

Predictive frameworks designed through the application of artificial intelligence (AI) modeling can pragmatically deliver more accurate forecasts of UV exposure metrics that are adaptable to changing physical conditions in the atmosphere and useful to users of mobile technology. Machine learning (ML) and deep learning (DL) algorithms are widely used AI-based forecasting systems that are cost-effective, robust and user-friendly for time-dependent forecasting [13]. Recent studies reveal that the DL technology is gaining more prominence in its application, particularly in the *UVI* forecasting framework where simulations of *UVI* forecasts have captured high predictive accuracy [14,15]. However, the DL models have a black-box architecture with hidden internal workings that are highly complex and non-explainable. To better understand the DL black-box-generated outcomes, most recent studies have utilized explainable artificial intelligence (xAI) architecture [16,17]. The xAI architectures enable the DL models to become transparent, as the outcomes are interpretable and more trustworthy for the end users and decision-makers [16]. A plethora of innovative research methodologies has applied the model-agnostic tools in the xAI domain that include the local and global model explainability. At the local level, the local interpretable model-agnostic explanations (LIME) technique robustly explains the individual prediction of the black-box model [18]. In regards to global explanations, the Shapley additive explanations (SHAP) and permutation feature importance (PFI) frameworks are capable of explaining the entire decision of the black-box predictive model [19]. The applications of xAI technique further allow the layperson to clarify the logic underlying the process of decision-making by a black-box model. Currently, there appears to be a significant gap in the literature on integrating xAI in modeling *UVI*, as no previous studies have applied the xAI architecture in the *UVI* forecasting framework.

This paper focuses on designing an xAI-based enhanced *UVI* forecasting system using DL technology to offer local and global explainability regarding the influence of the predictor variables on model outcomes. Solar zenith angle (SZA) is one important attribute that influences the level of solar UV radiation on the earth's surface. This variable is known to govern the optical path length while the incident radiation traverses through the earth's atmosphere [5]. At any given SZA, the unbroken cloud cover condition is another meteorological variable that significantly reduces the solar *UVI* by 50 to 60% and even more during precipitation [20]. However, the scattering of solar irradiation by partial intermittent cloud cover can cause an escalated spike in ground-level UV radiation, thus exceeding the nominal cloud-free surface UV radiation [5]. In this scenario, the general public can be subjected to more severe UV exposure, which poses even greater damaging effects on the skin and eyes. Aerosols are another important atmospheric variable that impacts the surface-level *UVI* [15]. Furthermore, the *UVI* is also affected by absorption and scattering due to stratospheric ozone [21].

The objective of the current study is to design an enhanced joint hybrid explainable deep neural network (DNN) to deliver more accurate short-term forecasts of solar *UVI* using satellite-derived variables (including SZA as a ground-based variable) and the partial autocorrelation function (PACF) of the *UVI* data generated at the most significant lags. Our model is an enhanced joint hybrid (EJH) for the reason that a dual-phase feature selection is carried out, followed by an application of Bayesian optimization to enhance the model performance. A remarkable xAI framework (denoted as X) is further utilized to offer local and global model explanations.

Thus, this objective model is denoted as EJH-X-DNN. The primary contributions of this paper are summarized as follows:

- A robust DL architecture, known as DNN is proposed and applied to a *UVI* forecasting domain using satellite-derived and ground-based datasets for four Australian hotspots (Darwin, Alice Springs, Townsville and Emerald) with high solar UV radiation.
- Dual-phase feature selection is employed for dimensionality reduction. In the first phase, the informative attributes are selected using model-specific feature importance by integrating random forest (RF) as the base model. In the second phase, the redundant predictors are identified and eliminated with respect to high correlation (r).
- Further enhancement of the predictive performance is achieved through efficient tuning of the model hyperparameters using a Bayesian optimizer (BO).
- Model-agnostic xAI is applied to interpret the predictive behavior of the model, where LIME is used to explain the model outcomes at the local level, while SHAP and PFI are used for explanations at the global level.
- The accurate and interpretable forecasts of short-term *UVI* by the predictive framework can facilitate the end-users to deliver more precise sun protection behavior recommendations to the general public and mitigate UV-exposure-related skin and eye health risks.

The remainder of the paper is organized as follows: Section 2 reviews the background and related literature; Section 3 discusses the theoretical overview of the focused concepts; Section 4 describes the different methods adopted in designing an explainable *UVI* forecasting system; Section 5 presents the results and deliberates related discussions; Section 6 discourses the concluding remarks of this study and future research directions.

## 2. Related works

Conventional mechanistic methods with instruments such as spectroradiometers and radiometers have been commonly utilized by most health sectors to extract UV exposure information and deliver timely sun protection advice to the general public [22]. However, the real-time application of these devices can be constrained by the high costs of equipment, installation, calibration and maintenance [5]. With such flaws and the issue of accessibility for most remote locations, an alter-

native deterministic method has been applied in developing the *UVI* forecasting framework. Though the deterministic approach seems to be promising, limitations caused by the use of estimated and assumed fixed initial conditions continue to affect the overall prediction accuracy [5,23].

The advent of AI-inspired expert predictive systems can robustly address the drawbacks of mechanistic and deterministic methods, particularly in forecasting solar *UVI*. The AI-based ML and DL forecasting platforms are known to exhibit immense computational efficiency and these algorithms are highly skillful in handling the non-linearity in input datasets [14]. The potential of the ML technique has been explored by [24] in forecasting long-term *UVI* on a global scale using a feed-forward multi-layered artificial neural network (ANN). Additionally, an extreme learning machine integrated with SZA was applied by [5] to forecast short-term *UVI* for a study site in Toowoomba, Australia. However, other studies have opted to employ DL technology over the ML approach, as the former employs a non-linear model of multiple hidden layer architecture that enables the framework to learn the complex relationship between outputs and inputs [25]. The ML technique also entails some overfitting issues [26]. In a recent work, three days ahead *UVI* was forecasted in a global context by exploiting a DL long short-term memory (LSTM) network [27]. Similarly, the daily *UVI* was forecasted for the state of Western Australia using a hybrid DL convolution long short-term memory (CNN-LSTM) network [14]. In another study, a wavelet hybrid convolutional LSTM (convLSTM) network was integrated with sky images and SZA in forecasting multi-step *UVI* for a Toowoomba-based study site in Australia [15].

In terms of model interpretability, none of the aforementioned predictive systems have applied xAI to extract model-agnostic local and global explanations that are instrumental in understanding the influences of different attributes on *UVI* predictions. Some relevance may be drawn from a recent study where an xAI-inspired model-agnostic SHAP and PFI explainers were integrated with a RF model to offer global interpretations based on interactions of the feature variables in predicting solar radiation [28]. Another similar research applied the LIME model-agnostic tool to extract local explanations for heat demand forecasting using different configurations of the LSTM networks [18]. SHAP explanation technique was also integrated with LSTM networks to analyze the global influence of input variables on energy consumption forecasting [29]. A recent survey highlighted that the SHAP explainer displays powerful performance in generating global post-hoc explanations based on the input perturbations using DNN [30].

The model-agnostic LIME, SHAP and PFI explainers have their separate strengths and shortcomings. The LIME technique is highly effective in delivering local post-hoc explanations by exploiting surrogate interpretable and reliable representations that best approximate the reference predictive model [31]. In comparison with SHAP, LIME is faster in execution as the latter algorithm generates instance-based interpretations [32]. On the positive side, the SHAP method efficiently offers explanations for the entire decision of the reference model at a global level. Although the SHAP tool can elegantly offer global explanations, the execution time of the algorithm is a bit high [17]. Keeping in mind the benefits of LIME and SHAP explainers, most researchers have opted to implement these methods simultaneously to extract more rigorous and faithful black-box model interpretations both at local and global levels for better decision-making [16,17]. Furthermore, PFI is another remarkable algorithm that provides black-box model explanations at the global level. However, like the SHAP tool, the PFI method also takes a slightly higher execution time to generate effective model explainability [33].

As mentioned earlier, a knowledge gap has been identified as the model-agnostic xAI architectures are not yet integrated with any DL black-box model to offer local and global explanations. Henceforth, the current study advocates a more comprehensive combination of LIME, SHAP and PFI explainers to provide model transparency, as well as to overcome any embedded biases of the *UVI* simulating black-box model

for better decision-making. Through xAI decision support tools, more reliable and credible sun-exposure behavior recommendations can be delivered to the public in the risk zone.

## 3. Methodology

In this study, the design phase of DL hybrid explainable *UVI* forecasting framework entails multiple modeling stages. The flowchart presented in Fig. 1 summarizes the significant stages affiliated with the modeling of *UVI* forecasts. In accordance with the flow chart summary, the first stage involves retrieval of satellite-derived and ground-based predictors plus the target variable for the four Australian hotspots with high UV radiation exposure. The second stage involves pre-processing and imputation of extracted datasets. In the third stage, the cross-correlation and partial auto-correlation of the features and the label are determined at the most significant hourly lag. The fourth stage entails dual-phase feature selection, where the first phase involves an application of a model-specific feature selection technique with RF and in the second phase the redundant features are eliminated on the basis of having higher r. In stage five, a DL hybrid explainable EJH-X-DNN model is designed and benchmarked with competing counterparts to forecast hourly ahead *UVI*. A BO is further applied to fine-tune the model hyperparameters. To assess the performance of the proposed EJH-X-DNN model against the benchmarked models, robust statistical score metrics are used. In the final stage, we exploit xAI-based model-agnostic tools (LIME, SHAP and PFI) to offer local and global explanations based on the black-box EJH-X-DNN model predictions.

Hereafter, the sub-sections provide a detailed methodology of the aforementioned stages involved in constructing the DL hybrid explainable *UVI* forecasting system.

### 3.1. Study site and data extraction

To establish and validate the merits of the proposed hybrid explainable EJH-X-DNN model in generating hourly forecasts of *UVI*, four Australian hotspots that are at high risk of harmful exposure to solar UV radiation are selected.

Table 1 shows the geographical description of the study sites and the inferential statistics of *UVI*. Two of these study sites are Darwin and Alice Springs from the Northern Territory (NT) while the other two are Townsville and Emerald from the State of Queensland (QLD). These hotspots are known to be subtropical regions that receive a large number of sunshine hours on an annual basis [5]. The health sector within these hotspots is significantly burdened by UV-exposure-related impacts on skin and eye health. Table 1 (a) details the geographical description of the four selected research hotspots.

In constructing the proposed model pipeline to forecast hourly horizon *UVI*, the first stage involves data extraction. The Australian Radiation Protection and Nuclear Safety Agency (ARPANSA) provided the ground data for the target variable *UVI*, which has been accessed from https://www.arpansa.gov.au and for all four Australian hotspots. Considering that one unit of *UVI* is equivalent to 25 mW m⁻² of erythemally effective irradiance [20,5], *UVI* is mathematically represented as:

$$UVI = \frac{1}{25 \text{ mW m}^{-2}} \int_{290}^{400} S(\lambda) \cdot E_{UV}(\lambda) \cdot d\lambda, \tag{1}$$

where $E_{UV}$ is the spectral energy in W m⁻² nm⁻¹ measured over the terrestrial wavelengths of 290 to 400 nm, and $S(\lambda)$ is the relative erythema effectiveness at each discrete wavelength. To ensure cost-effectiveness and accurate procedure, the ARPANSA data is closely monitored by regular data assessment and quality checks. For each selected site, Table 1 (b) presents the inferential statistics of ARPANSA-sourced *UVI* in terms of mean, standard deviation, median, maximum value, minimum value, skewness and kurtosis. All the statistical descriptions are very significant. For instance, the *UVI* values showing low kurtosis indicate
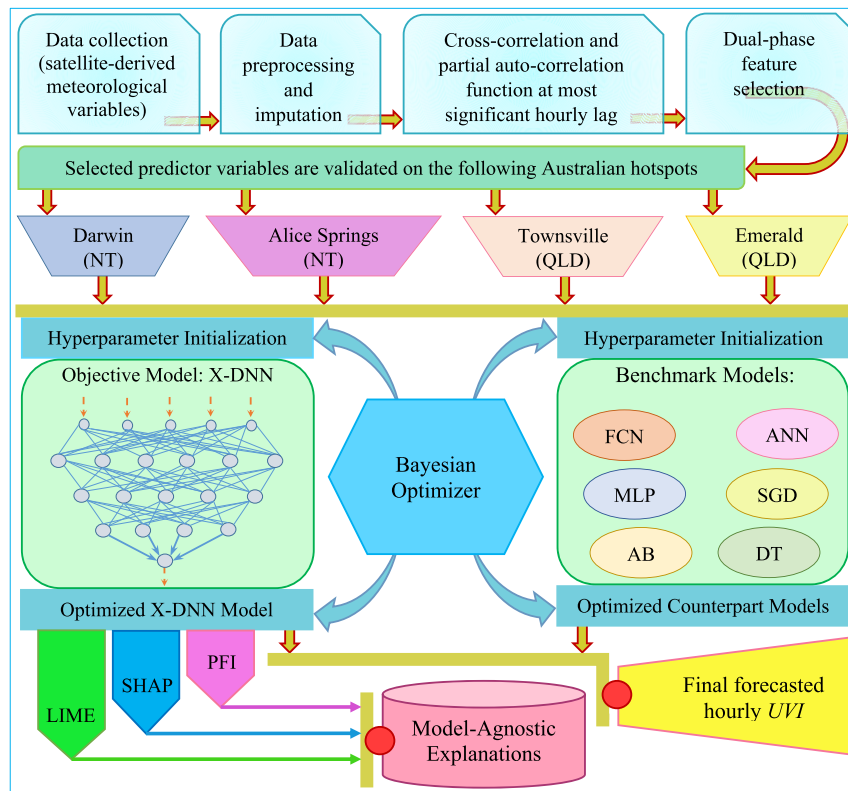
**Fig. 1.** Flowchart highlighting the major stages in the design phase of proposed hybrid EJH-X-DNN model for generating hourly ahead forecasts of *UVI* with model-agnostic explanations.

**Table 1**
(a) The geographical description of the study sites, (b) Inferential statistics of *UVI*.

| (a) Site Name, State | Location | | |
|---|---|---|---|
| | Latitude (°E) | Longitude (°E) | Elevation (m) |
| Darwin, NT | 12.43 | 130.89 | 28 |
| Alice Springs, NT | 23.80 | 133.89 | 576 |
| Townsville, QLD | 23.53 | 148.16 | 15 |
| Emerald, QLD | 19.33 | 146.76 | 189 |

| (b) Target Variable | Location | Mean | St. Dev. | Median | Max. | Min. | Skewness | Kurtosis |
|---|---|---|---|---|---|---|---|---|
| *UVI* | Darwin | 4.99 | 3.72 | 4.45 | 16.63 | 0.01 | 0.53 | -0.62 |
| | Alice Springs | 4.72 | 3.67 | 3.97 | 16.72 | 0.01 | 0.71 | -0.45 |
| | Townsville | 4.69 | 3.57 | 3.89 | 16.65 | 0.03 | 0.80 | -0.17 |
| | Emerald | 4.50 | 3.45 | 3.86 | 16.20 | 0.01 | 0.78 | -0.20 |

that the datasets are light-tailed relative to a normal distribution. Having light-tailed distribution implies a lack of outliers in the overall *UVI* dataset.

In selecting the model inputs, satellite-derived predictors have been sourced from the National Aeronautics and Space Administration (NASA) database, particularly the Goddard Online Interactive Visualization and Analysis Infrastructure (GIOVANNI) geoscience data repository from https://giovanni.gsfc.nasa.gov/giovanni/. GIOVANNI acquires data for over 2000 satellite variables, for which it eminently provides online-based visualizations and analytical platforms [34]. Due to the inadequacy of ground-based datasets, most meteorological problems have been alternatively addressed using satellite-based remote sensing data [35].

For the purpose of this study, we preferably adopted the satellite-derived products captured by the Modern-Era Retrospective Analysis for Research and Applications (MERRA) satellite to simulate forecasts of hourly horizon *UVI*. Considering that the variations in incident UV radiation are significantly interconnected with cloud cover conditions,

ozone effects, atmospheric aerosol column, dust concentrations and content of water vapor [5,36], eight relative predictor variables were extracted from the MERRA satellite for fusion with the proposed DL *UVI* simulating framework.

Additionally, the ground-based SZA that is known to highly affect the intensity of solar UV-radiation was acquired by integrating a deterministic Pro6UV method [5]. Table 2 details the eight MERRA-derived predictors and the ground-based SZA with corresponding acronyms, data extraction source, units, instrument/model for data acquisition and spatial resolution in degrees.

To construct the hybrid explainable EJH-X-DNN model, two years of datasets for the aforementioned ground-based and satellite-derived meteorological variables were extracted from 1st January 2020 to 31st December 2021, as indicated in Table 3. These datasets were extracted at a time resolution of 1 hour from 7.30 am to 4.30 pm on a daily basis. After having extracted these important meteorological parameters, the *UVI* (target input) and the nine predictors (feature inputs) datasets were ready for further preprocessing toward modeling *UVI*.

**Table 2**

Description of the input features (ground-based and satellite-derived) used to construct the proposed hybrid explainable EJH-X-DNN model.

| Attribute Name | Acronym | Source | Units | Instrument/Model | Spatial Resolution |
|---|---|---|---|---|---|
| Solar zenith angle | SZA | Ground | ° | Pro6UV | - |
| Cloud area fraction for high clouds | CAFHC | MERRA-2 | - | M2T1NXRAD v5.12.4 | 0.5°×0.625° |
| Cloud area fraction for middle clouds | CAFMC | MERRA-2 | - | M2T1NXRAD v5.12.4 | 0.5°×0.625° |
| Cloud area fraction for low clouds | CAFLC | MERRA-2 | - | M2T1NXRAD v5.12.4 | 0.5°×0.625° |
| Total aerosol angstrom parameter | TAAP | MERRA-2 | - | M2T1NXAER v5.12.4 | 0.5°×0.625° |
| Total aerosol scattering AOT | TAS | MERRA-2 | - | M2T1NXAER v5.12.4 | 0.5°×0.625° |
| Dust scattering AOT | DS | MERRA-2 | - | M2T1NXADG v5.12.4 | 0.5°×0.625° |
| Total column ozone | TCO | MERRA-2 | Dobsons | M2T1NXSLV v5.12.4 | 0.5°×0.625° |
| Total precipitable water vapor | TPWV | MERRA-2 | $kg\,m^{-2}$ | M2T1NXSLV v5.12.4 | 0.5°×0.625° |

**Table 3**

Site-based segregation of input datasets into training, validation and testing during the model design phase.

| Sites | Period | Data Points | Training Points (≈80%) | Validation Points | Testing Points (≈20%) |
|---|---|---|---|---|---|
| Darwin | 01-Jan-2020 to 31-Dec-2021 | 7265 | 5815 | | 1450 |
| Alice Springs | 01-Jan-2020 to 31-Dec-2021 | 7267 | 5815 | 10% of | 1452 |
| Townsville | 01-Jan-2020 to 31-Dec-2021 | 7276 | 5817 | Training | 1459 |
| Emerald | 01-Jan-2020 to 31-Dec-2021 | 7273 | 5815 | | 1458 |

## 3.2. Data preprocessing

The second stage of *UVI* modeling for the four sites in Australia entails data preprocessing. It was important to carefully scrutinize the extracted datasets to locate any missing data. There were very few instances when some datasets were missing and these were duly recovered by imputing with the monthly median of the respective variable at the same daily time domain. For this study, the median imputation technique among the three imputation methods of mean, median and listwise deletion was adopted. Imputation using the median approach is robust and generates more accurate imputed values in comparison with the mean and listwise deletion methods [37]. Once the complete sets of data were obtained through imputation, the stationarity in these datasets was further tested by applying the augmented Dickey-Fuller Test [38]. The test outcome disclosed that all the input datasets were stationary for the four hotspots.

In the third stage, the cross-correlation coefficient ($r_{cross}$) and partial autocorrelation function (PACF) were assessed with the aid of correlogram plots to obtain time-lagged inputs at the most significant lag for modeling *UVI*. For instance, Fig. 2 (a) illustrates the $r_{cross}$ plots to investigate the co-variances between *UVI* and feature variables for the Darwin hotspot. A 95% confidence band was used as a reference where the lags of any variable within this boundary were considered insignificant. After evaluating $r_{cross}$ of each feature with *UVI*, the most significant historically preceding values of the predictor variables were selected as inputs to construct the proposed hourly ahead *UVI* forecasting system for all four sites.

Fig. 2 (b) presents the PACF plot of the *UVI* time series that displays the antecedent behavior in terms of hourly lags of *UVI* for the Darwin hotspot. After analyzing the PACF of *UVI* time series, the four most significant antecedent lagged *UVI* were considered as model inputs. For the purpose of this study, the four antecedent lags of *UVI* at $t$ - 1, $t$ - 2, $t$ - 3 and $t$ - 4 are denoted as PACF1, PACF2, PACF3 and PACF4, respectively, where $t$ represents real-time. The time-lagged inputs for the other three sites of Alice Springs, Townsville and Emerald were also extracted via assessment of $r_{cross}$ and PACF in a similar manner. Thereafter, a historical lagged matrix was created for the ground-based and satellite-derived predictors at a lag of ($t$ - 1) as inputs toward feature selection for each site.

## 3.3. Feature selection

The fourth stage of model building involves dual-phase feature selection of the ground and satellite-acquired predictor variables. In the first phase, a wrapper-based model-specific approach was exploited to select the most pertinent attributes. The feature datasets were first subjected to a base ML model to search the space of all possible subsets of the feature inputs in terms of their importance. In this study, a RF model is applied as the base ML model to fit the attribute datasets and assess all possible combinations with respect to the evaluation criterion in selecting the most informative features. After evaluation, the base model ranked the input predictor variables in accordance with their overall importance to the model.

Fig. 3 shows the model-specific feature importance generated by the base model for the four selected sites. With respect to the displayed ranked attributes, the base model has considered SZA as the most pertinent feature with the highest importance score for each selected site. The criterion was to eliminate any inapt predictor variable that captures zero feature importance scores. As per the feature selection outcomes described in Fig. 3, it is observed that none of the attributes within the feature space yielded zero feature importance scores for all four sites. Consequently, all the features were considered important using the model-specific feature selection approach.

Having none of the attributes eliminated from the feature set in the first phase, the study adopted a second phase of filter-based feature selection by assessing the degree of correlation between the attributes within the feature space. The correlations among the nine predictor variables of the four sites are described with an aid of a color-coded heatmap in Fig. 4.

The criterion was to drop one of the attributes having a high correlation, preferably r > 0.8 or r < -0.8 for this study. Any two predictor variables displaying high correlation become redundant as they contribute very similar information towards model training and eliminating one of them improves the computational efficiency. In conformity with Fig. 4, none of the features were observed to be redundant for all four sites. No two attributes among the feature space captured high correlations as per the selection criteria and for this reason, all the features were considered pertinent inputs for the model construction phase. Together with the selected feature variables, the four historical lagged
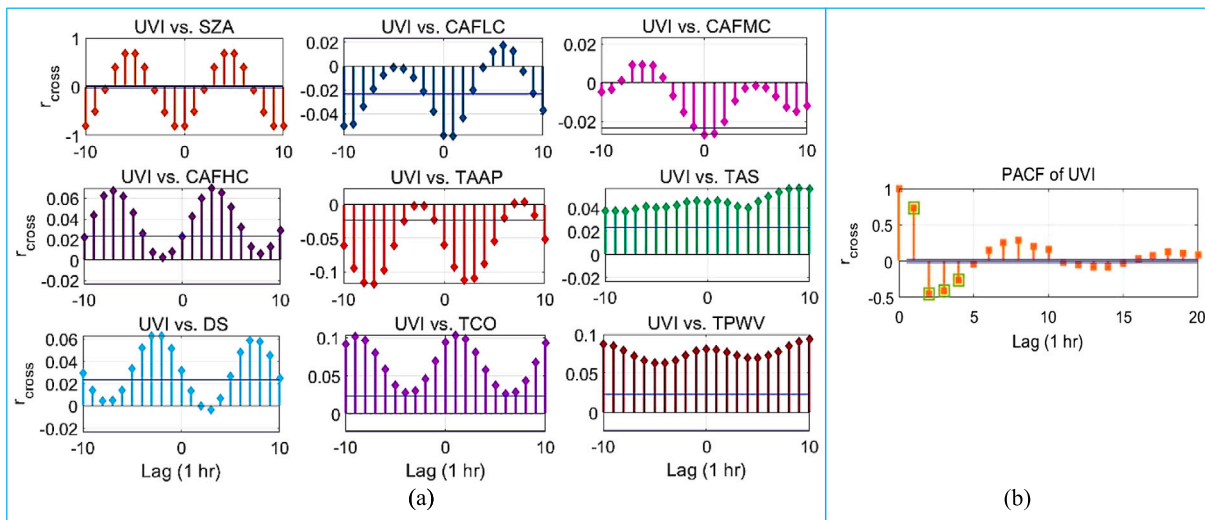
**Fig. 2.** Hourly lagged correlograms showing (a) cross-correlation coefficient ($r_{cross}$) for *UVI* versus the nine predictor variables (acronyms described in Table 2) for the Darwin site, (b) Partial autocorrelation function (PACF) of the *UVI* series showing the four most significant lags for the Darwin site.
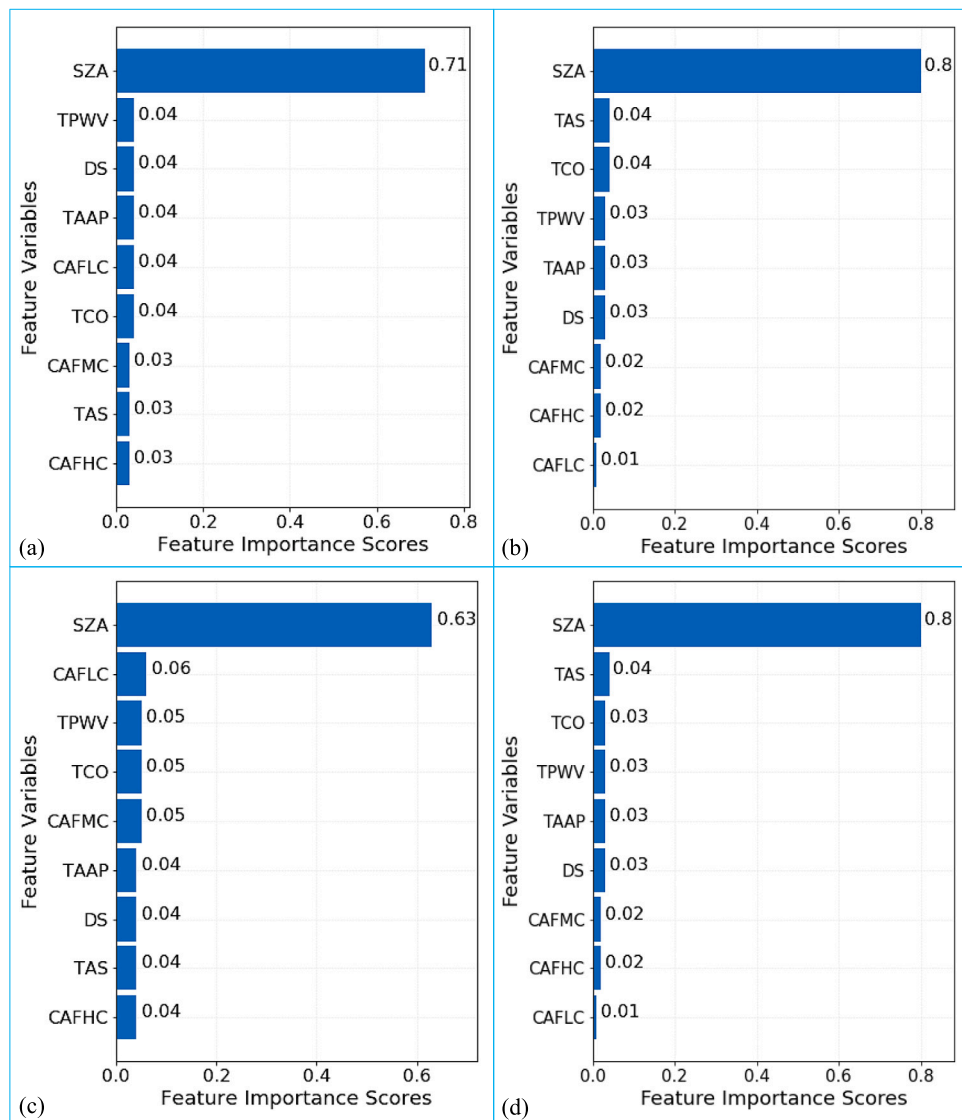


**Fig. 3.** First phase of feature selection using model-specific feature importance with the base model of random forest for (a) Darwin, (b) Alice Springs, (c) Townsville and (d) Emerald; where any predictor variable having feature importance scores equal to zero is eliminated from the design phase of the hybrid EJH-X-DNN model.
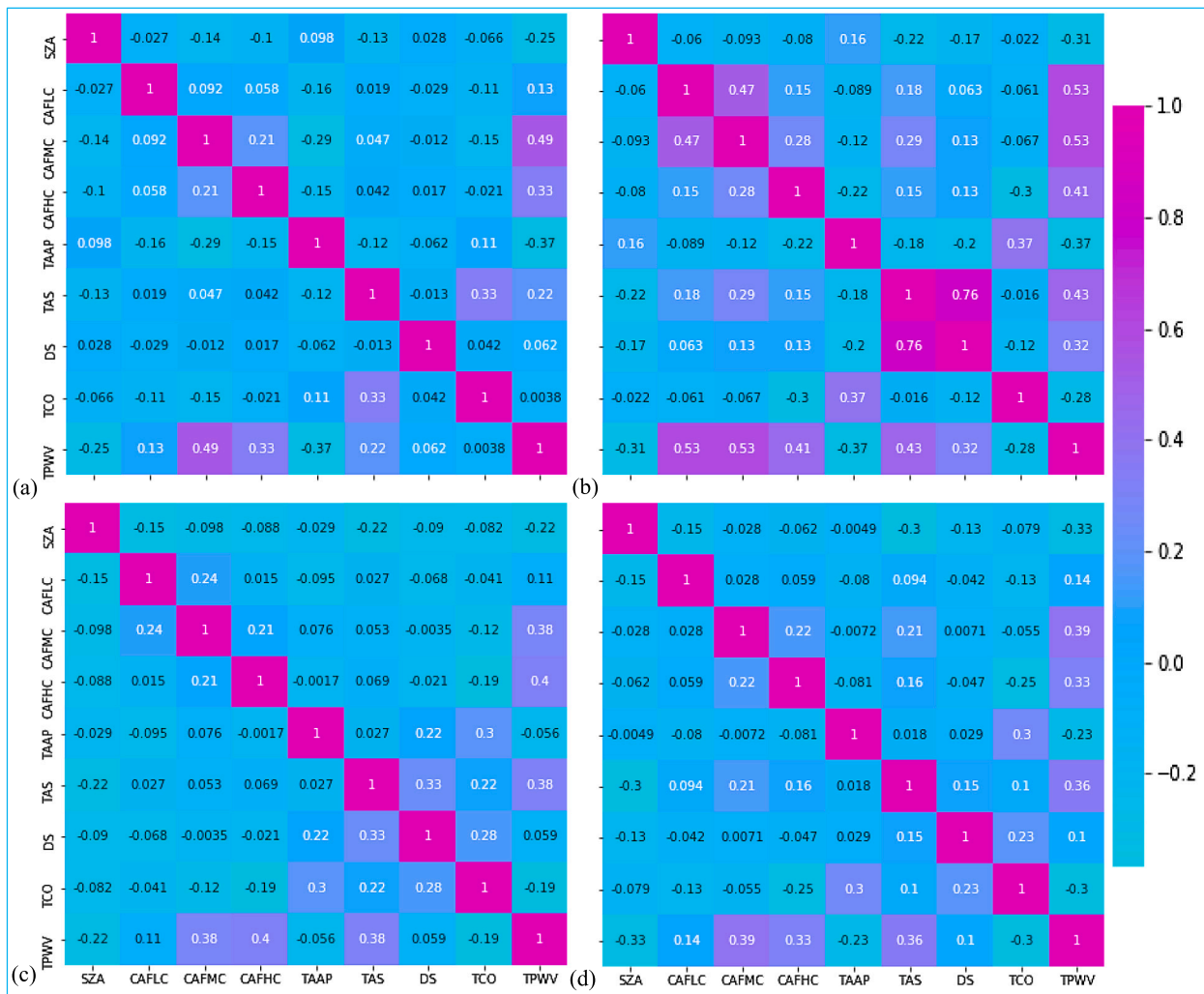
**Fig. 4.** Second phase of feature selection using a color-coded heat map highlighting a visual overview of low, average and high correlation (r) of the predictor inputs considered for (a) Darwin, (b) Alice Springs, (c) Townsville and (d) Emerald; where any two variables having high r (preferably r > 0.8 or r < -0.8 for this study) are regarded redundant and one of them is eliminated from the design phase of the hybrid explainable EJH-X-DNN model.

memories of *UVI* (PACF1, PACF2, PACF3 and PACF4) were applied as overall inputs towards simulating the next hourly *UVI* series.

### 3.4. Design of the UVI predictive model

In the fifth stage, the actual hybrid explainable EJH-X-DNN model is designed. For developing the model pipeline, an eminent Python programming language was implemented via a Google Colab platform with a freely available Jupyiter Notebook interface supported by a tensor processing unit (TPU) and graphical processing unit (GPU). The virtual environment of the powerful python tool provides remarkable packages for the execution of ML and DL algorithms, which include Scikit-learn [39], Keras [40] and TensorFlow [41]. Additionally, the MATLAB programming tool was employed for plotting the correlograms of the predictand and predictors [42].

Prior to feeding the target and predictor inputs to the model, the datasets were normalized in the range of [0-1] so that each variable would exhibit the same order of magnitude. This was achieved by applying a min-max normalization [43], defined as follows:

$$X_{NORM} = \frac{X_{ACT} - X_{MIN}}{X_{MAX} - X_{MIN}}, \qquad (2)$$

where $X_{NORM}$ is normalized input data, $X_{ACT}$ is actual input data, $X_{MIN}$ is the minimum value and $X_{MAX}$ is the maximum value. Through the normalization process, stable convergence of biases and

weights is guaranteed for efficient training and testing of the predictive model [44].

Consequently, a train-test split was carried out by partitioning the input datasets into training, validation and testing, as shown in Table 3. Data segregation is a critical phase of model building as the forecasting capability and overall feasibility of the predictive model are largely dependent on the partitioning ratio. Since there is no standard rule for data partitioning, this study adopts an earlier research strategy [45,46] to segregate 80% of the site-based input datasets for training and 20% for testing. Additionally, 10% of the training data was utilized for model validation, primarily to overcome the issues regarding model biases via a 10-fold cross-validation approach. On the same notion, the modeling constraints led by over-fitting can also be addressed using the cross-validation process [47]. While partitioning, the training and testing datasets were cut-off using date-time to ensure that the future patterns of the training set do not leak into the testing set.

The scope of this study was to design a hybrid explainable EJH-X-DNN model that could simulate more accurate forecasts of hourly horizon *UVI* with local and global model-agnostic interpretability based on the influences of the input features on predicted outcomes. For comprehensive benchmarking of the newly proposed model, we further designed some skillful competing models, which include EJH-FCN, EJH-ANN, EJH-MLP, EJH-AB, EJH-SGD and EJH-DT. The designations of the

**Table 4**

Designations of the enhanced joint hybrid deep learning and machine learning models developed to simulate hourly ahead forecasts of *UVI*.

| Model Type | | Model Designation |
|---|---|---|
| Proposed xAI Model: | Enhanced Joint Hybrid Explainable DNN | EJH-X-DNN |
| | | |
| Benchmarked Models: | Enhanced Joint Hybrid FCN | EJH-FCN |
| | Enhanced Joint Hybrid ANN | EJH-ANN |
| | Enhanced Joint Hybrid MLP | EJH-MLP |
| | Enhanced Joint Hybrid AdaBoost | EJH-AB |
| | Enhanced Joint Hybrid SGD | EJH-SGD |
| | Enhanced Joint Hybrid DT | EJH-DT |

objective model along with the benchmarked models are distinctly described in Table 4.

In constructing the EJH-X-DNN model, a robust DL DNN was integrated as a suitable base model. The DL-based models are less explored in *UVI* forecasting and their supremacy over conventional ML-based models is well known [15]. A DNN is an extension of an ANN that is constructed by concatenating three principle layers in the architecture: an input layer, one or more fully connected hidden layers and an output layer [48]. The depth of DNN architecture is defined by the number of hidden layers and each layer of the network has available one or more interconnected artificial neurons. By having networks of multiple hidden layers and nodes in the design architecture, the DNN model automatically extracts relevant features or information from the input datasets [49]. For generating time-series predictions, the most suitable number of neurons in the output layer is one. A feed-forward mode is utilized for information processing, which begins from the input layer, goes through the hidden layers, and finally arrives at the output layers. For each layer, the inputs are multiplied by weights, followed by the addition of a bias to the sum of the resulting product. Mathematically, the neural network forward propagation model [45] can be best described as:

$$a_i^l = f\left(\sum_{j=1}^{N^{l-1}} w_{ij}^l a_j^{l-1} + b_i^l\right), \tag{3}$$

where $a_i^l$ is the output value from the $i^{th}$ neurons in the $l^{th}$ layer neural network, $a_j^{l-1}$ is the output value from the $i^{th}$ neurons in the $(l-1)^{th}$ layer neural network, $w_{ij}^l$ is the weight from the $j^{th}$ neurons in the $(l-1)^{th}$ layer to the $i^{th}$ neurons in the $l^{th}$ layer, $b_i^l$ is the bias term from the $i^{th}$ neurons in the $l^{th}$ layer neural network, $N^{l-1}$ is the number of neurons in the $(l-1)^{th}$ layer and $f(\cdot)$ is the activation function of the neurons.

A common DL DNN architecture comprising a feed-forward back propagation network (FFBPN) is applied in this study. Generally, the FFBPN in the architecture enables the model to efficiently learn and map the input-output relationships. Through the processes of learning and mapping, the model's weight and threshold values are adjusted so that the predictive error is minimized and the overall performance is optimized. Selection of an optimal number of hidden layers, neurons, activation functions (such as sigmoid function, hyperbolic tangent (tanh) function, rectified linear unit (ReLU) function and exponential linear unit (ELU) function) further optimizes the model performance [48]. Additionally, the issue of overfitting in DNN is significantly reduced by exploiting a regularization approach that includes a weight penalty and early stopping (or dropout) during model training [45]. In constructing the enhanced joint hybrid benchmarked models, the architecture of base models includes a fully convolutional network (FCN), artificial neural network (ANN), multilayer perceptrons (MLP), AdaBoost (AB), stochastic gradient descent (SGD) and decision tree (DT), respectively. The conceptual and architectural details of the benchmarked models are elucidated elsewhere, as these are well-known methods [50–55].

### 3.5. Hyperparameter tuning using Bayesian optimizer

While the DNNs exhibit superior performance capability, the forecasting accuracy can be affected by improper tuning of model hyperparameters during training and validation. To enhance the predictive performance, a powerful BO was applied with a Gaussian process surrogate algorithm for optimizing the hyperparameters of the DNN architecture. BO is an elegant hyperparameter tuning algorithm that directs the search for a global optimization problem based on Bayes' rule of conditional probability [56]. The Bayes' rule of conditional probability [57] is given as:

$$p(w|D) = \frac{p(D|w)\ p(w)}{p(D)}, \tag{4}$$

where $p(w|D)$ is the posterior distribution, $p(D|w)$ is the likelihood, $p(w)$ is the prior distribution, $p(D)$ is the marginal, $w$ is an unobserved quantity and $D$ is the input dataset.

The BO approaches the optimal point more efficiently than random sampling because the optimization process selects the values of the next iteration by considering the outcomes of prior iterations [56]. In comparison with other common optimization techniques such as grid search and random search, BO has higher hyperparameter tuning efficiency [58]. For grid and random search, each evaluation in its iterations is independent of prior iterations. In such cases, the hyperparameter search space regions with unsatisfactory performance are unavoidably assessed, which finally leads to high computational costs.

During optimization, the BO fits a surrogate function over an unknown objective function using randomly selected data points. A highly robust and flexible Gaussian process [59], which is also utilized for the purpose of this study, forms the posterior distribution over the objective function to consequently update the surrogate function. In this instance, an acquisition function is generated using the posterior distribution to explore new regions within the search space, as well as to make use of the regions captured with optimal results [60]. These processes continue to feed the surrogate model with updated outcomes and terminate just after meeting a pre-defined stopping criterion. In this case, the acquisition function, known as the expected improvement (EI) [58] is applied where the criterion is to maximize this function to locate the next sampling point. The EI is given as:

$$\text{EI}(\theta) = \frac{P_{good}\ (\theta)}{P_{bad}\ (\theta)}, \tag{5}$$

where $P_{good}$ is the probability that $\theta$ is in the good group, $P_{bad}$ is the probability that $\theta$ is in the bad group and $\theta$ represents the hyperparameter set.

Table 5 details the search space and the optimal architecture of the proposed model that includes the number of neurons in the input layer and hidden layers, batch size, number of epochs, activation function, optimizer, learning rate and the parameters of the backpropagation algorithm ($\beta_1$, $\beta_2$ and Epsilon) for the four selected sites. The input layer of DNN architecture was selected using the dual-phase feature selection approach. To achieve a deep architecture of DNN, four hidden layers were utilized. The output layer was assigned a single neuron to generate the predicted *UVI*. While we selected a good learning rate of 0.001,

**Table 5**
Optimal architecture of the hybrid explainable EJH-X-DNN model and the competing counterparts designed to generate hourly ahead *UVI* forecasts.

| Predictive Models | Hyperparameters | Search Space | Optimal Hyperparameters | | | |
|---|---|---|---|---|---|---|
| | | | Darwin | Alice Springs | Townsville | Emerald |
| EJH-X-DNN | Input neurons | [100, 110, 120] | 100 | 120 | 100 | 110 |
| | Hidden neurons 1 | [70, 80, 90] | 70 | 70 | 90 | 90 |
| | Hidden neurons 2 | [40, 50, 60] | 60 | 60 | 40 | 40 |
| | Hidden neurons 3 | [20, 25, 30] | 20 | 25 | 30 | 20 |
| | Hidden neurons 4 | [5, 10, 15] | 10 | 10 | 15 | 15 |
| | Batch size, Epochs | [200, 300], [150, 200] | 200, 150 | 200, 150 | 200, 200 | 200, 200 |
| | Activation function | [ReLU] | ReLU | | | |
| | Optimizer, Learning rate | [Adam], [0.001] | Adam, 0.001 | | | |
| | $\beta_1$, $\beta_1$, Epsilon | [0.9], [0.999], [$1\times10^{-10}$] | 0.9, 0.999, $1\times10^{-10}$ | | | |
| EJH-FCN | Filters 1 | [50, 80, 100] | 80 | 100 | 80 | 50 |
| | Filters 2 | [40, 50, 60] | 50 | 40 | 60 | 50 |
| | Filters 3 | [20, 30, 40] | 30 | 40 | 30 | 40 |
| | Batch size, Epochs | [200, 300], [150, 200] | 300, 150 | 200, 150 | 200, 200 | 200, 150 |
| | Activation function | [ReLU] | ReLU | | | |
| | Optimizer, Learning rate | [Adam], [0.001] | Adam, 0.001 | | | |
| | $\beta_1$, $\beta_1$, Epsilon | [0.9], [0.999], [$1\times10^{-10}$] | 0.9, 0.999, $1\times10^{-10}$ | | | |
| EJH-ANN | Input neurons | [100, 110, 120] | 100 | 110 | 110 | 100 |
| | Hidden neurons | [30, 40, 50] | 40 | 50 | 50 | 40 |
| | Batch size, Epochs | [200, 300], [150, 200] | 200, 200 | 300, 200 | 200, 200 | 300, 200 |
| | Activation function | [ReLU] | ReLU | | | |
| | Optimizer, Learning rate | [Adam], [0.001] | Adam, 0.001 | | | |
| | $\beta_1$, $\beta_1$, Epsilon | [0.9], [0.999], [$1\times10^{-10}$] | 0.9, 0.999, $1\times10^{-10}$ | | | |
| EJH-MLP | Hidden layer sizes | [30, 50, 80] | 50 | 80 | 80 | 80 |
| | Learning rate init | [$1\times10^{-5}$, $1.5\times10^{-5}$] | $1.5\times10^{-5}$ | $1.5\times10^{-5}$ | $1.5\times10^{-5}$ | $1.5\times10^{-5}$ |
| | Maximum iteration | [1000, 2000, 3000] | 3000 | 3000 | 3000 | 3000 |
| | Tol | [$1\times10^{-8}$, $1.5\times10^{-8}$, $2\times10^{-8}$] | $1\times10^{-8}$ | $1.5\times10^{-8}$ | $1.5\times10^{-8}$ | $2\times10^{-8}$ |
| | Activation function | [ReLU] | ReLU | | | |
| | Solver, Alpha | [Adam] , [0.0001] | Adam, 0.0001 | | | |
| | $\beta_1$, $\beta_1$, Epsilon | [0.9], [0.999], [$1\times10^{-10}$] | 0.9, 0.999, $1\times10^{-10}$ | | | |
| EJH-AB | n estimators | [100, 200, 300] | 100 | 100 | 200 | 200 |
| | Learning rate | [1.0, 1.5, 2.0] | 1.0 | 1.0 | 1.0 | 1.0 |
| | Loss | [linear] | linear | | | |
| EJH-SGD | Eta0 | [0.01, 0.02, 0.03] | 0.03 | 0.03 | 0.02 | 0.03 |
| | Power_t | [0.25, 0.30, 0.35] | 0.25 | 0.25 | 0.25 | 0.25 |
| | Maximum iteration | [500, 1000, 1500] | 1000 | 1500 | 1500 | 1000 |
| | Tol | [0.001, 0.002, 0.003] | 0.002 | 0.001 | 0.001 | 0.001 |
| | Alpha | [0.0001] | 0.0001 | | | |
| EJH-DT | Minimum samples split | [2, 4, 6] | 6 | 6 | 4 | 6 |
| | Maximum depth | [5, 10, 15] | 5 | 15 | 5 | 10 |
| | Minimum samples leaf | [1, 5, 10] | 5 | 10 | 10 | 10 |
| | Maximum features | ['auto', 'sqrt', 'log2'] | 'auto' | | | |

the activation function was selected as ReLU. To further handle the issue of over-fitting, an early stopping technique was employed through monitoring the model performance during the validation phase. The BO algorithm was also implemented to tune the hyperparameters of the counterpart models, for which the search details and optimized architectures are described in Table 5.

### 3.6. Model performance criteria

The study applied a range of performance metrics for rigorous evaluation of the newly constructed EJH-X-DNN model against the benchmarked models in forecasting hourly ahead *UVI* for the four Australian sites. The set of these statistical metrics includes Pearson's Correlation Coefficient (*r*), Mean Absolute Error (*MAE*), Root Mean Squared Error (*RMSE*) and the Legate-McCabe Efficiency Index (*LME*) [23,61]. Mathematically, these metrics can be represented as:

$$r = \frac{\sum_{i=1}^{N}\left(UVI_i^O - \overline{UVI}^O\right)\left(UVI_i^F - \overline{UVI}^F\right)}{\sqrt{\sum_{i=1}^{N}\left(UVI_i^O - \overline{UVI}^O\right)^2}\sqrt{\sum_{i=1}^{N}\left(UVI_i^F - \overline{UVI}^F\right)^2}}, \quad (6)$$

$$RMSE = \sqrt{\frac{1}{N}\sum_{i=1}^{N}(UVI_i^O - UVI_i^F)^2}, \quad (7)$$

$$MAE = \frac{1}{N}\sum_{i=1}^{N}\left|UVI_i^O - UVI_i^F\right|, \quad (8)$$

and

$$LME = 1 - \frac{\sum_{i=1}^{N}\left|UVI_i^O - UVI_i^F\right|}{\sum_{i=1}^{N}\left|UVI_i^O - \overline{UVI}^O\right|}, \quad (9)$$

where $N$ is the total number, $UVI_i^O$ and $UVI_i^F$ are observed and forecasted *UVI* for the $i^{th}$ observation, $\overline{UVI}^O$ and $\overline{UVI}^F$ are average observed and average forecasted *UVI*. The values of $r$ range between -1 to +1, where the two extremes are ideal values. The error values of *MAE* and *RMSE* range from 0 to $\infty$, where 0 and $\infty$ imply a perfect fit and worst fit, respectively. The *LME* can robustly address the predictive limitations and it ranges between 0 to 1, where 1 is an ideal value.

## 3.7. Explainability of model outcomes

In the next stage, xAI-based model-agnostic tools were exploited to explain the predictions of the newly designed EJH-X-DNN model for the four hotspots. To extract local explainability, the LIME algorithm was applied to reveal the instance-based local impact of respective predictor variables fed in the *UVI* simulating system. To obtain global explainability, the SHAP and PFI tools were applied.

## 3.8. xAI-based local interpretable model-agnostic explanations (LIME)

The LIME algorithm is an eminent xAI tool that efficiently explains the predictions of a regression or classification "black-box" model by approximating it locally with a surrogate interpretable model [62]. To generate model explanations, LIME supports three formats of input datasets that include image, text and tabular data [63]. For the current study, LIME is applied with a tabular data format to derive local interpretability. The model explanations offered by LIME allow the end users to understand and interpret the predictive decisions. The LIME-defined explanation [64] is given as:

$$\xi(x) = \underset{g \in G}{\text{argmin}} \, \mathcal{L}(f, g, \pi_x) + \Omega(g), \tag{10}$$

where $f$ denotes the explained black-box model, $\pi_x$ is the proximity measure defining the neighborhood size around instance $x$, $G$ represents the set of interpretable models, $\mathcal{L}(f, g, \pi_x)$ is the measurement of the unfaithfulness of explanation model $g$ in approximating prediction of the original black-box model $f$, and $\Omega(g)$ component measures the complexity of the explanation for all $g \in G$. The first goal is to have a low $\Omega(g)$ component so that the model is simple enough to offer better interpretability. The second and major goal is to minimize the $\mathcal{L}(f, g, \pi_x)$ component to achieve an interpretable approximation of the original reference model.

LIME enumerates local explanations that highlight the contribution of individual feature variables toward the black-box prediction of a sample data [16]. In accomplishing this, LIME replicates the feature data by perturbing the input observations several times, thereafter generating a prediction with the black-box model based on the perturbed data. By benchmarking the perturbed data with the original data point, LIME determines the Euclidean distance between them. Finally, LIME uses the calculated distance of the original observation from the perturbed data point and indicates which input features are useful for the black-box model in generating predictions.

## 3.9. xAI-based Shapley additive explanations (SHAP)

SHAP algorithm robustly extracts global explanations in terms of interactions and influences of the feature variables on decisions of a black-box model in delivering predictions [65]. For this purpose, the SHAP tool is deployed to enhance the global interpretability of the *UVI* predictive framework. The foundation of SHAP is derived from the concept of Shapley value in game theory, which has a major goal of fairly distributing the players' contributions in achieving a particular outcome collectively [66,67]. Similarly, Shapely values can be applied in black-box models, to quantify the contribution of individual predictor variables for generating predictions. For a given predictor, $X_j$ in a black-box model, the SHAP value [66,65] is given as:

$$Shapely(X_j) = \sum_{S \subseteq N \setminus \{j\}} \frac{k! \, (p - k - 1)!}{p!} \, (f(S \cup \{j\}) - f(S)), \tag{11}$$

where $N \setminus \{j\}$ defines the set of all possible combinations of feature variables excluding $X_j$, $S$ represents a feature set in $N \setminus \{j\}$, $p$ denotes the total number of features, $f(S)$ represents the black-box model prediction with features in $S$ and $f(S \cup \{j\})$ represents the black-box model prediction with both features in $S$ and feature $X_j$. The $Shapely(X_j)$

represents the SHAP value of a feature, which is the weighted average of the marginal contribution over all possible models with different combinations of feature variables [66]. Though SHAP takes up some computational time in executing, the process utilizes all the subsets of the input data to deliver consistent, transparent and more accurate global interpretations. For the purpose of this study, a skillful kernel explainer was utilized while implementing the SHAP algorithm to reveal the impact of the predictor variables on the overall decisions and predictions of the proposed hybrid explainable model.

## 3.10. Permutation feature importance (PFI)

PFI is another effective xAI tool that is model-agnostic and offers global explanations for the black-box processes in generating predictions. Basically, the PFI is determined by permuting the values of a predictor variable $i$, followed by the calculation of the increment in prediction error due to this permutation [28]. The PFI score ($PFI_s$) is given as:

$$PFI_s = e^p - e^o, \tag{12}$$

where $e^o$ is the estimated original model error and $e^p$ is the calculated new error after permuting the values of the feature variable $i$. A feature with a large PFI score has a higher influence on the model's predictions. PFI can be executed with different error functions, yet the common ones are mean absolute error (*MAE*) and root mean square error (*RMSE*) [28, 68]. For this study, PFI is applied with an error function of *MAE* to globally explain the decisions of the DL *UVI* predictive system.

## 4. Results

This section consolidates the extensive performance evaluation and model-agnostic explanations of the prescribed EJH-X-DNN model to demonstrate the superiority of the proposed *UVI* forecasting tool against six benchmarked models that include EJH-FCN, EJH-ANN, EJH-MLP, EJH-AB, EJH-SGD and EJH-DT. To appraise the merits of the proposed model based on the statistical score metrics described in (6)-(9) and visual plots, all models were meticulously assessed for generating hourly horizon forecasts using the testing datasets for four solar-rich hotspots in Australia. Table 6 enumerates the testing phase performance of the EJH-X-DNN model against the comparative counterparts for all four sites. Almost all the experimentally captured modeling statistics reveal that the objective model outperforms the competing counterpart models in forecasting *UVI* with the highest Pearson's correlation coefficient ($r$), lowest root mean square error (*RMSE*) and lowest mean absolute error (*MAE*) for all four hotspots. The proposed model demonstrates superior forecasting capability for each of site by yielding the highest accuracies (i.e. $r = 0.897$ - $0.960$; *RMSE* $= 1.071$ - $1.638$; *MAE* $= 0.633$ - $1.081$) against its counterparts (i.e. $r = 0.842$ - $0.954$; *RMSE* $= 1.139$ - $2.025$; *MAE* $= 0.682$ - $1.641$). We aver that our hybrid explainable EJH-X-DNN model approaches the best predictive precision by capturing $r$ values that approach 1, *RMSE* values that approach 0 and *MAE* values that approach 0 as well.

The assessment of the newly constructed EJH-X-DNN model using the most stringent performance indicator of the Legate-McCabe Efficiency Index (*LME*) further revealed its outstanding performance in Fig. 5. For almost all the hotspots, the objective model yields the highest values of *LME* (i.e. *LME* $= 0.652$ - $0.804$) and outshines the comparative models (i.e. *LME* $= 0.466$ - $0.789$). Having captured the highest *LME* statistics indicates that the proposed model exhibits the lowest stringent errors in forecasting short-term *UVI*.

Consequently, the xAI-inspired model-agnostic tools were applied to robustly offer explanations on the predictive contributions of the input variables that included satellite-derived predictors, ground-based predictors and the antecedent lagged memory of *UVI*. The satellite-derived xAI inputs for this research include cloud cover effects (i.e. CAFHC,

**Table 6**

Testing phase performance of the newly designed EJH-X-DNN model against the counterpart models in terms of correlation coefficient (*r*), root mean square error (*RMSE*) and mean absolute error (*MAE*) in forecasting hourly ahead *UVI* for the four sites.

| *UVI* Forecast Model | Darwin | | | Alice Springs | | | Townsville | | | Emerald | | |
|---|---|---|---|---|---|---|---|---|---|---|---|---|
| | *r* | *MAE* | *RMSE* | *r* | *MAE* | *RMSE* | *r* | *MAE* | *RMSE* | *r* | *MAE* | *RMSE* |
| EJH-X-DNN | 0.900 | 1.638 | 1.081 | 0.960 | 1.071 | 0.633 | 0.897 | 1.601 | 1.068 | 0.913 | 1.359 | 0.883 |
| EJH-FCN | 0.889 | 1.865 | 1.239 | 0.950 | 1.273 | 0.809 | 0.872 | 1.840 | 1.342 | 0.906 | 1.462 | 1.036 |
| EJH-ANN | 0.898 | 1.659 | 1.069 | 0.954 | 1.139 | 0.682 | 0.891 | 1.675 | 1.114 | 0.903 | 1.473 | 0.930 |
| EJH-MLP | 0.888 | 1.729 | 1.133 | 0.950 | 1.179 | 0.704 | 0.871 | 1.777 | 1.271 | 0.878 | 1.631 | 1.112 |
| EJH-AB | 0.871 | 1.966 | 1.598 | 0.910 | 1.872 | 1.569 | 0.842 | 2.025 | 1.641 | 0.864 | 1.771 | 1.410 |
| EJH-SGD | 0.889 | 1.713 | 1.138 | 0.947 | 1.214 | 0.757 | 0.866 | 1.798 | 1.315 | 0.870 | 1.658 | 1.170 |
| EJH-DT | 0.882 | 1.776 | 1.177 | 0.946 | 1.228 | 0.708 | 0.869 | 1.793 | 1.262 | 0.875 | 1.701 | 1.040 |
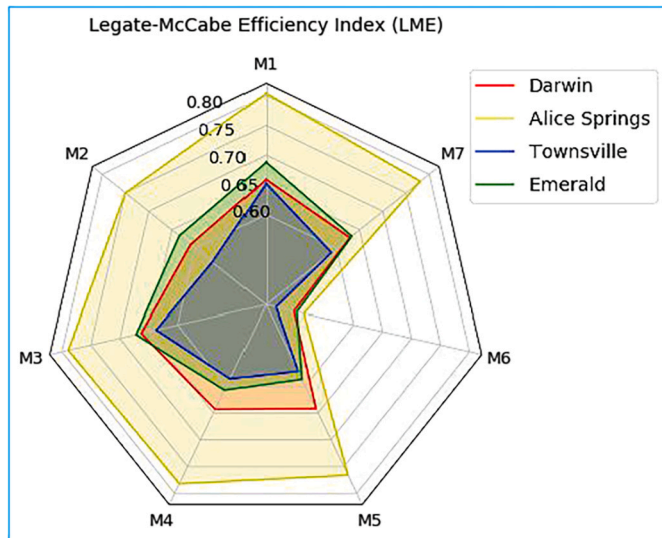


**Fig. 5.** Rader plot of the Legate-McCabe Efficiency Index (*LME*) elucidating the performance of the newly designed EJH-X-DNN model (M1) alongside the competing benchmarked models of EJH-FCN (M2), EJH-ANN (M3), EJH-MLP (M4), EJH-SGD (M5), EJH-AB (M6) and EJH-DT (M7) in forecasting *UVI* for the four selected sites.

CAFMC and CAFLC), aerosol scattering (i.e. TAS and TAAP), ozone effect (i.e. TCO), dust particles (i.e. DS) and water vapor (i.e. TPWV). Other xAI inputs include the ground-based predictor of solar zenith angle (i.e. SZA) and the antecedent lagged memory of *UVI* at lags of $t$ - 1, $t$ - 2, $t$ - 3 and $t$ - 4 (i.e. PACF1, PACF2, PACF3 and PACF4) for all the selected sites.

To retrieve the local explanations on the predictions of the hybrid explainable model, the study applied an elegant LIME model-agnostic framework. In this study, the number of LIME-explainable instances was equal to the number of hourly *UVI* datum points in the testing data series that ranged from instance 0 to instance 5815. For the purpose of visualization, the LIME-generated local explainability analysis on instance-based prediction is displayed in Fig. 6 for instance 25 and instance 175. The local interpretability presented with the aid of bar graphs reflects individual feature contributions towards the forecasting of these instances for the four Australian hotspots that have high ground-level UV exposures. On the bar graphs, the y-axis displays the features with corresponding feature values, while the x-axis shows the relative strengths of individual features in terms of their numerical contributions. The attributes that have increased or supported the predicted value of the *UVI* forecast are emphasized in green. Conversely, the attributes that have decreased or negatively impacted the predicted instance are highlighted in red. Additionally, the predicted value of *UVI* is represented on a bar in orange color.

The comparisons of LIME outputs at instance 25 and instance 175 for the Darwin, Alice Springs and Townsville sites in Fig. 6 (a)-(c) reveal that the feature attributes of PACF1 and SZA are the major contributors

towards the outcome of *UVI* forecasting. However, for the Emerald site in Fig. 6 (d), PACF1 is the major contributor in predicting *UVI* for both instances. Moreover, SZA shows a positive effect on *UVI* predictions for all four hotspots. It is also observed that PACF1 has contributed positively for most instances, except for instance 175 of the Darwin site and instance 25 of the Emerald site, where the predictive contributions were negative. As per the LIME values presented on the x-axis, PACF1 is the largest predictive contributor at instance 175 for the Alice Springs and Emerald site where PACF1 > 6.38 strongly envisages the outcome of the *UVI* forecast. However, as per instance 25 of Emerald site where 1.52 < PACF1 < 3.71, it has the highest negative effect on this predictive outcome. SZA is shown to be largely responsible for the prediction outcomes for both instances at the Darwin site. At this site, SZA > 30.21° highly favors the prediction outcome. Other predictors that include TCO, PACF3, TPWV, CAFMC and CAFHC also displayed significant predictive contributions at different sites. The overall outputs of the LIME tool offer substantial instance-based local interpretations that can boost the trustworthiness of the hybrid explainable EJH-X-DNN model.

For extracting the global explanations on the entire predictions of the hybrid explainable model, the study applied a classic SHAP model-agnostic framework. The SHAP feature importance bar plots presented on the left-hand side in Fig. 7 illustrate the mean absolute Shapley values of individual features on the x-axis and the ranked input features on the y-axis. These attributes are ranked by prioritizing the features with larger absolute Shapley values. The SHAP summary violin plots presented on the right-hand side in Fig. 7 display the feature effects of the ranked attributes based on the feature importance. In outlining the violin plot, each instance equal to the number of hourly *UVI* datum points in the testing data series is plotted with the corresponding Shapley value for each feature attribute on the x-axis against ranked input features on the y-axis. The feature value at each instance is denoted by different colors with pink and light blue representing high and low feature values, respectively. The higher feature values of all the predictor variables denoted in pink imply positive Shapley values that highly contribute towards the outcome of *UVI* prediction. In contrast, the lower feature values shown in light blue have negative Shapley values that do not favor the outcome of predicted *UVI*.

The inforgraphics presented in Fig. 7 reveals that PACF1 and SZA have the most impact on the outcome of the *UVI* forecast for all four Australian hotspots. For the Darwin site in Fig. 7 (a), SZA contributes more than PACF1 towards the predictive outcome on the Shapley scale. However, PACF1 is more dominant in impacting the outcome of predicted *UVI* for the Alice Springs, Townsville and Emerald hotspots in Fig. 7 (b)-(d). For these highly impactful predictors, the higher feature values in pink favor the outcomes of *UVI* predictions, while those in light blue with lower values of features do not favor the predicted outcomes. Together with PACF1 and SZA, other influential attributes on *UVI* predictions include TCO, PACF3, TPWV, PACF2, CAFMC and CAFLC for most sites. It is further observed that the importance of the DS attribute is negligible on the SHAP summary plots for all four hotspots. Further descriptions of the variations in model predictions
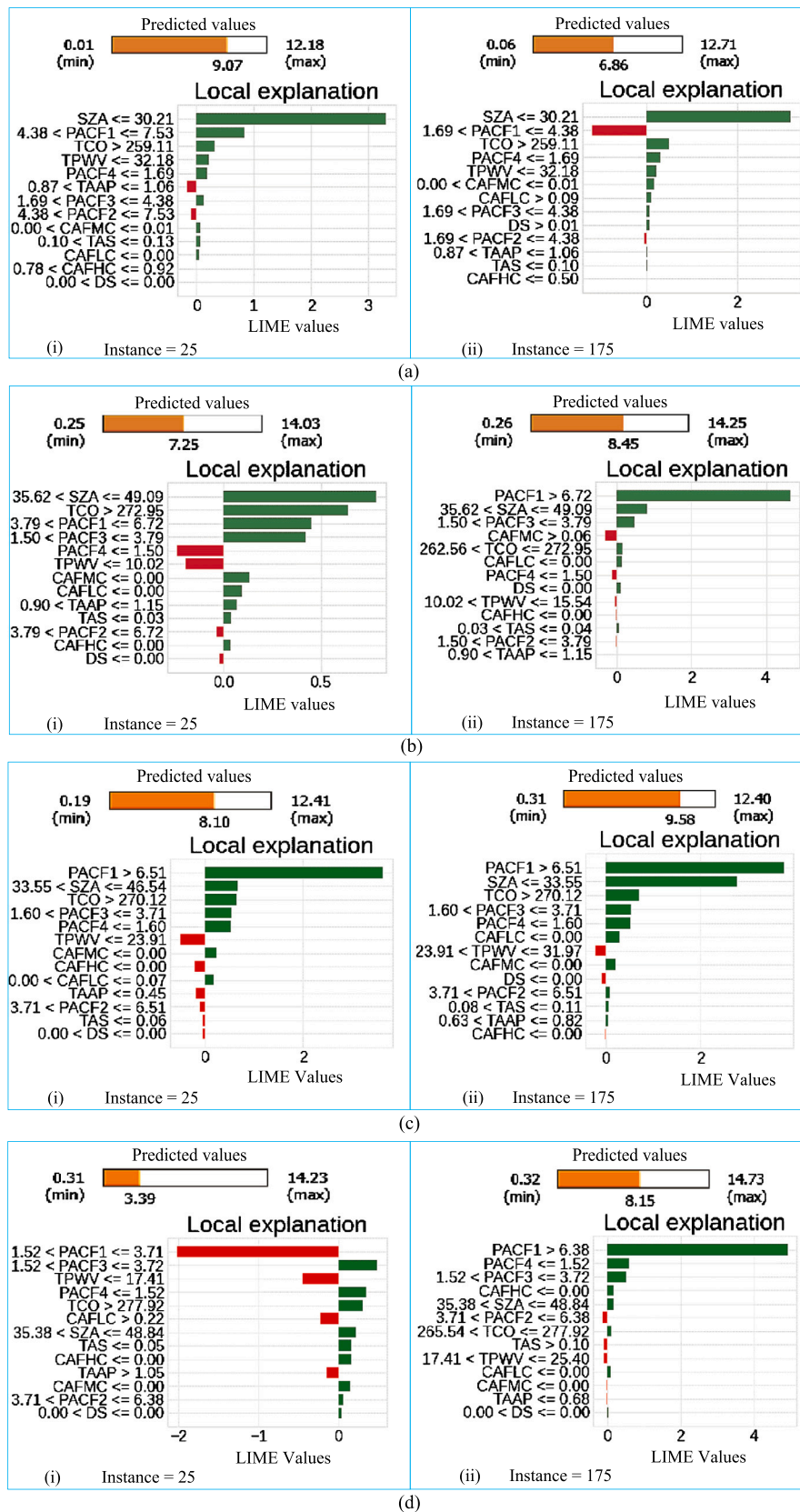
**Fig. 6.** LIME explanation bar plots at (i) instance 25 and (ii) instance 175 for the sites (a) Darwin, (b) Alice Springs, (c) Townsville and (d) Emerald, where the green bars indicate that the features have a positive impact on the model (increase the model score) and the red bars indicate that the features have a negative impact on the model (decrease the model score).

with respect to the feature importance values and respective feature interactions can be obtained using a SHAP dependence plot.

The SHAP dependence plots shown in Fig. 8 can help understand the marginal effect of two attributes on the predicted outcome of the hy-
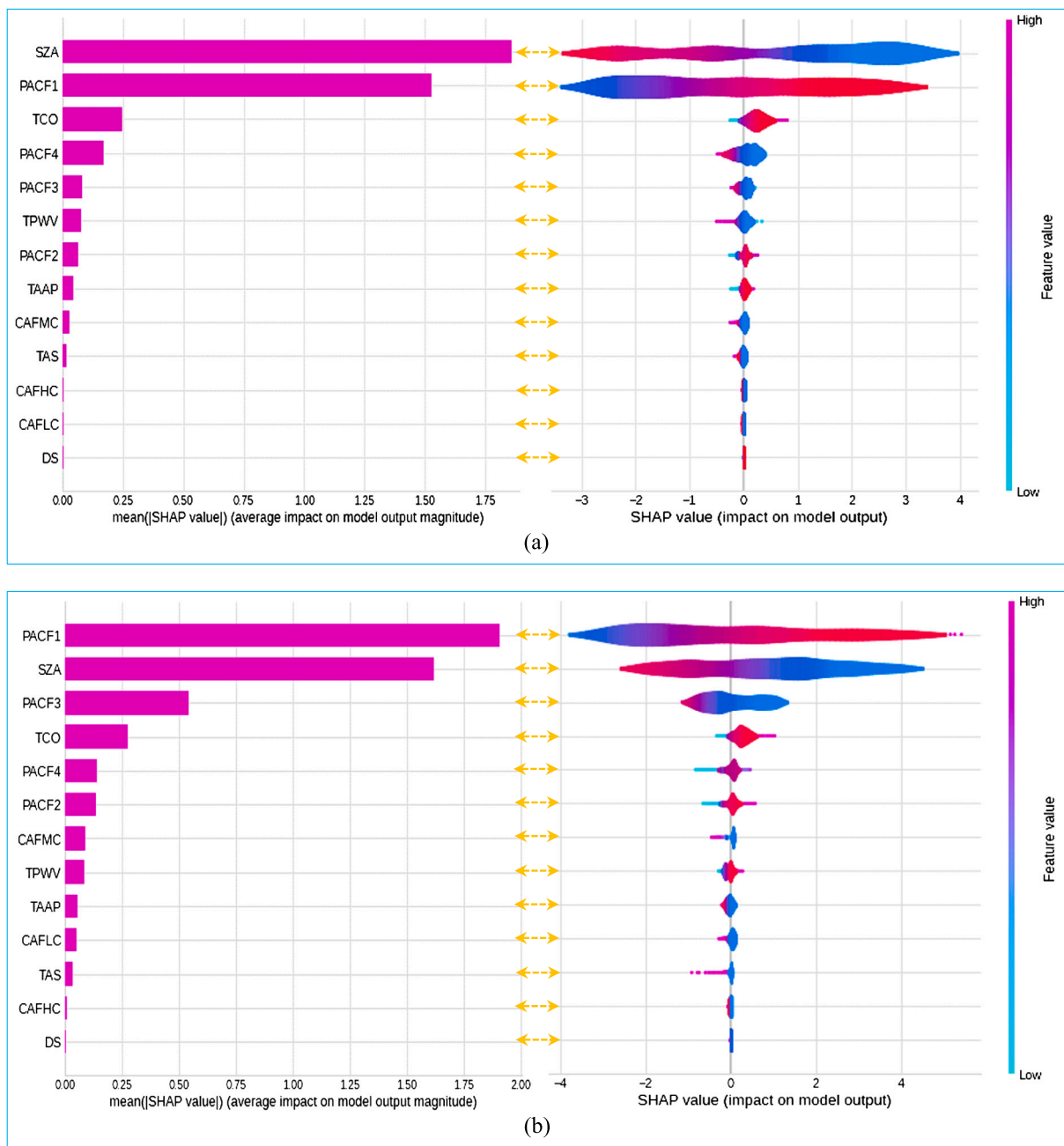
**Fig. 7.** SHAP feature importance bar plots and SHAP summary violin plots for the sites (a) Darwin, (b) Alice Springs, (c) Townsville and (d) Emerald.

brid explainable EJH-X-DNN model. For the purpose of this study, these plots were utilized to explore the testing phase interactions between the most influential predictor variables i.e. PACF1 and SZA towards the model prediction outcomes. For the Darwin hotspot, the SHAP dependence plot in Fig. 8 (a) reveals that the predicted values of *UVI* are more likely to be favored when SZA < 47° and PACF1 values are high. In the case of the Alice Springs site, the SHAP dependence plot in Fig. 8 (b) indicates that with SZA < 52° and high values of PACF1, it is more likely that the predicted *UVI* values are favored. Similarly, interactions between these two features in Fig. 8 (c) show that the predicted *UVI* values are more likely to be favored at high values of PACF1 and SZA < 36° for the Townsville site. Moreover, the predicted *UVI* values for the Emerald hotspot in Fig. 8 (d) are more likely to be favored when SZA < 46° and PACF1 values are high. For all the sites, it is observed that the feature interactions between the two most influential predictor variables of SZA and PACF1 highly favor the prediction outcomes of the

proposed EJH-X-DNN model at lower values of SZA and higher values of PACF1.

For further veracity and comparisons of the global interpretable results generated by SHAP, a prominent PFI model-agnostic framework was applied. The PFI bar plots presented in Fig. 9 rank the predictor variables with respect to their PFI values and illustrate that SZA and PACF1 are the most influential attributes in impacting the prediction outcomes of the newly developed EJH-X-DNN model. It is observed that the results of the PFI bar plots and the SHAP summary plots (Fig. 7) are almost in conformity. According to the PFI plots, Fig. 9 (a) and Fig. 9 (c) reveal that the most impactful features for the Darwin and Townsville site are SZA and PACF1, while TAS and DS have very less impact on the prediction outcome. Fig. 9 (b) shows that PACF1 and SZA are the most influential predictor variables, while TAAP has the least influence in predicting *UVI* for the Alice Springs hotspot. For the Emerald hotspot in Fig. 9 (d), PACF1 and SZA are the most important attributes in gen-
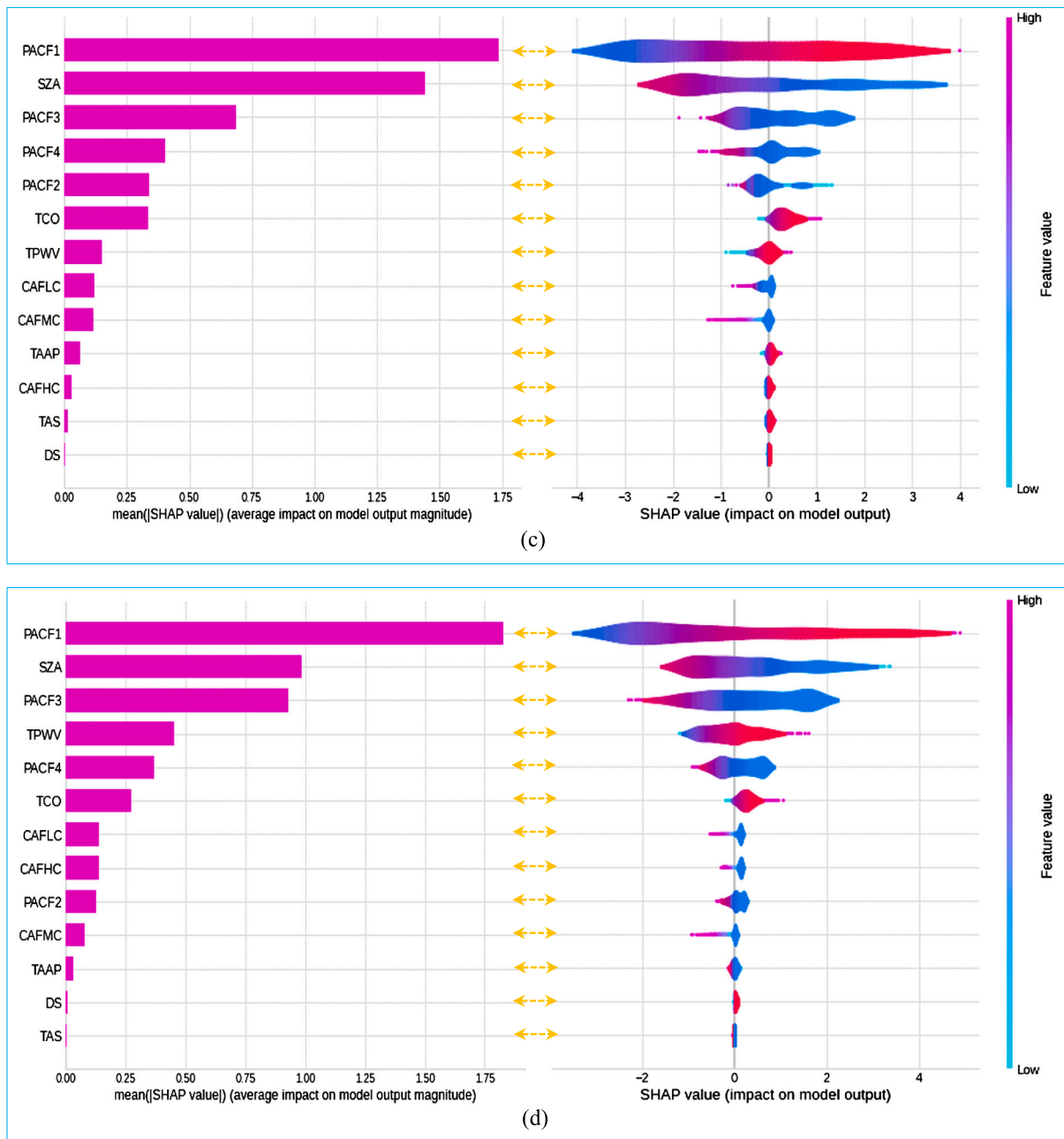
Fig. 7. (*continued*)

erating *UVI* prediction outcomes, while TAAP and DS show the lowest importance. The implementation of the PFI model-agnostic tool along with the SHAP framework offers more reliable and in-depth global explanations of the *UVI* prediction outcome by the proposed model for the usefulness of the end-users.

## 5. Discussion

The artificial intelligence predictive system designed in this study robustly forecasts short-term *UVI* to demonstrate its efficacy as a decision support tool that can deliver more accurate sun-exposure information to the public and help mitigate UV radiation-associated skin diseases and eye health ailments. The performance evaluation aptitudes, such as those illustrated in Table 6 and Fig. 5 offer compelling evidence to establish the hybrid explainable EJH-X-DNN model as a credible *UVI* forecasting system for all four Australian hotspots that are exposed to high ground-level UV radiation. Alongside the comparative mod-

els, the proposed model is the most superior forecasting framework as its assessment demonstrates high-performance efficiencies with all the performance measurement criteria. After testing on four different datasets of Darwin, Alice Springs, Townsville and Emerald hotspots, we further assert that the prescribed model exhibits remarkable forecasting stability as it captured the lowest error values of *RMSE* and *MAE* on almost all four datasets. Though the proposed model outperformed the benchmarked models for all four sites, it delivered the best site-based performance for the Alice Springs hotspot. The site-to-site variations in performance are largely led by the intermittent and stochastic nature of the cloud cover effects. For instance, the evaluation outcomes of the Darwin site have recorded slightly better *MAE* and *LME* values by the EJH-ANN model while the *r* and *RMSE* values are dominated by the proposed EJH-X-DNN model. Despite these subtle variations in performance, all other captured aptitudes affirm the prescribed model as the best overall performer in forecasting hourly ahead *UVI* for the four sites.
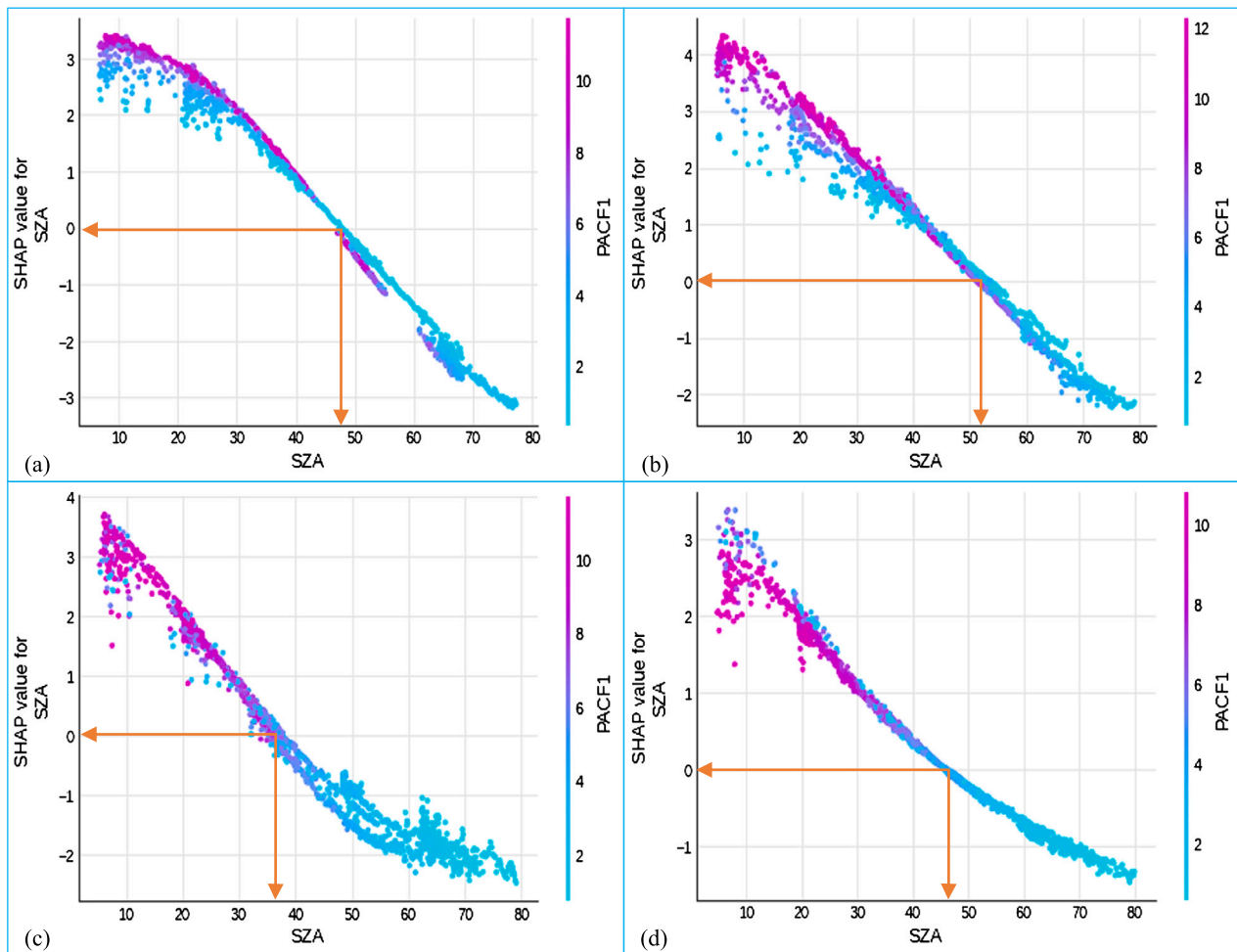
**Fig. 8.** SHAP dependence plots for interaction between SZA and PACF1, which are the most important features in the UVI forecasting framework for (a) Darwin, (b) Alice Springs, (c) Townsville and (d) Emerad.

Though the outcomes of the newly designed EJH-X-DNN model are promising, this study employed the xAI tool to further expand the model's transparency and reliability for its practical applications. According to the literature, some previous studies have developed AI-based ML and DL models to forecast solar *UVI* for different sites [14,5,27,15]. However, it is evident that none of the previous studies have designed a *UVI* forecasting system by integrating the xAI tool to explain the predictive outcomes of their models. Thus, by applying a model-agnostic xAI approach to offer the predictive explanations of the proposed DL "black-box" model, the current research fills this gap in the literature. Through the applications of xAI in this study, the "black-box" model interpretations of the decisions taken in simulating *UVI* forecasts were obtained both in terms of local and global explanations. [69] proposed the applications of the fascinating LIME, SHAP and PFI algorithms to extract local and global post-hoc explanations based on the input perturbations using a classification-based predictive model to classify oropharyngeal cancer. The current study also applied the xAI frameworks of LIME, SHAP and PFI, but with a major focus on explaining a forecasting-based model in predicting hourly horizon *UVI*.

The advantage of applying LIME is its ability to offer instance-based model explanations for the time-series *UVI* forecasting system developed in this study. LIME has the capacity to obtain better coverage values in terms of weighted sums so that the end users could easily comprehend how the predictions are made for each instance [17,64]. The applications of SHAP and PFI framework are also highly beneficial as these tools provide global explanations of the newly designed *UVI* forecasting system. The SHAP values based on coalitional game theory

capture the mean marginal contribution of individual feature attributes to the single prediction made by a "black-box" model [69]. Here, the motivation for the approach is that the SHAP-extracted explainable outcomes are statistically more reliable. For the purpose of this study, the SHAP xAI algorithm offers a complete explanation between the global average and the model output as the overall interpretation of the predicted *UVI*. Considering the PFI algorithm [28], this tool presents global explanations of the "black-box" model predictions by using the aggregated importance scores to account for the impact of feature attributes on the entire performance of the prescribed *UVI* simulating system. The study applied both the SHAP and PFI frameworks, to generate remarkable comparisons of the global explanations for the proposed *UVI* predictive system for the four Australian hotspots.

The overall instance-based model explanations acquired using LIME indicate that PACF1 and SZA are the two major contributors towards predicting short-term *UVI* for all four Australian hotspots. Similarly, the outcomes of SHAP and PFI tools have revealed PACF1 and SZA as the most impactful predictor variables in generating *UVI* predictions for these four hotspots. Further model explainability extracted using the LIME, SHAP and PFI xAI frameworks show that the contribution of the DS feature variable towards *UVI* predictions is very low. This indicates that the scattering of solar UV radiation by the atmospheric dust particles has very less impact on ground-level UV radiation. The analysis of the SHAP summary and feature importance plots highlight that the effect of the TAS attribute is also significantly low on the model predictions for almost all the sites. In terms of the cloud cover effects, the attributes of CAFMC and CAFLC show some significant influence on the
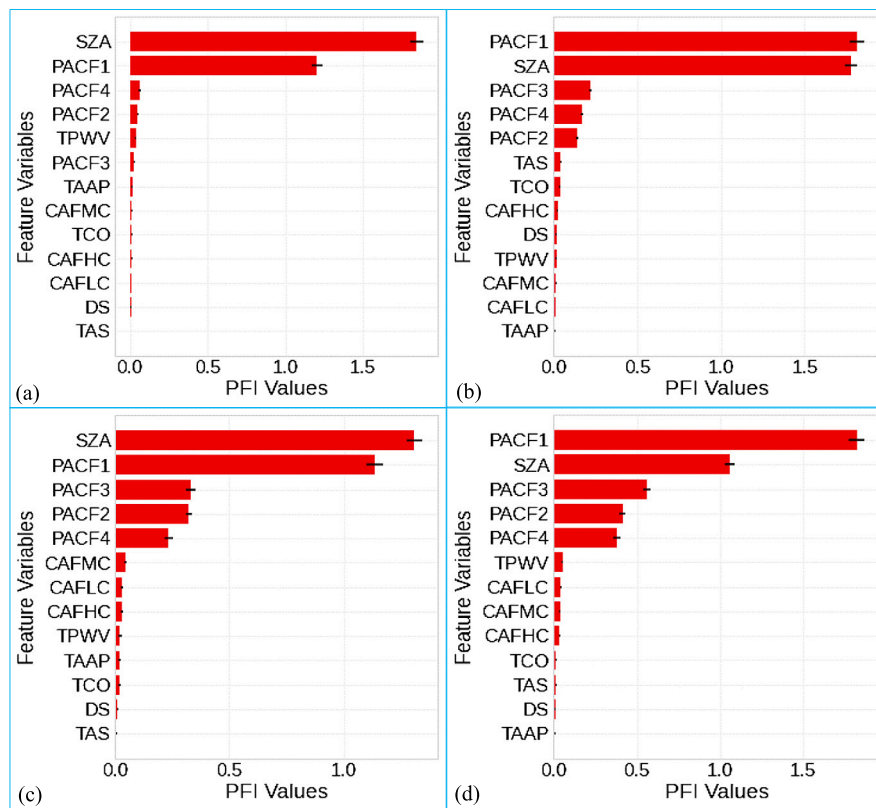
**Fig. 9.** Permutation feature importance (PFI) bar plots for (a) Darwin, (b) Alice Springs, (c) Townsville and (d) Emerald.

forecasted *UVI*. It is known that the scattering by partial cloud cover may cause a sudden escalated spike in the stochastic UV, which can exceed nominal cloud-free surface solar UV radiation [5]. The SHAP summary and feature importance plots offer vivid global explanations of how each attribute impacts the model decisions in generating the predictive outcomes of the *UVI* forecasts. The global explainability outcomes of the SHAP summary plots, together with the PFI results offer a generic overview of the ranked impacts that each feature has on the model forecasts.

The findings of forecasting performance and model explainability outcomes presented in this research have indicated remarkable practical applications of the newly designed EJH-X-DNN model to forecast short-term *UVI* by replacing the previously used mechanistic measurement and deterministic modeling techniques. It is known that the traditional mechanistic method is highly constrained by the issue of accessibility for most remote regions, along with high installation, operation and maintenance costs [15]. The proposed hybrid explainable EJH-X-DNN model can robustly substitute the mechanistic approach as it is potentially portable, cost-effective and user-friendly for the benefit of the end-users. Our proposed model can also substitute the conventional deterministic method that is constrained by the applications of assumed fixed initial conditions [5]. There are no assumed initial conditions being integrated into the architectural design of this hybrid explainable *UVI* forecasting framework.

The prescribed DL model trained with atmospheric variable datasets avers its practical utility in forecasting short-term *UVI* for most temperate countries, particularly for remote regions. For instance, our model trained with cloud cover conditions datasets can overcome the complex intermittency issue to successfully predict the cloud-affected *UVI*. It is known that the unbroken cloud cover condition attenuates the ground-level *UVI* by 50 to 60% and even more during precipitation [5]. However, under partial cloud cover conditions, the sudden spikes of scattered intermittent UV radiation are escalated above the nominal cloud-free surface solar UV radiation. Due to the significant influence

of stochastic cloud cover effects on the ground-level *UVI*, this study adopted a short-term forecasting horizon instead of a long-term to ensure that the escalated spikes of UV radiation are effectively captured. The proposed model is also trained with aerosol, ozone, dust scattering and precipitation datasets to enhance the forecasting capability and applicability of the hybrid explainable model for most geographical locations outside the range of the current ARPANSA network in Australia, as well as other temperate countries where the general public is at high risk of harmful UV exposure effects.

Considering the enhanced performance and ability to offer explainable outcomes, we have further exemplified the potential real-life application of the proposed *UVI* forecasting system in Fig. 10. The predictive system works on online and offline modes to deliver short-term forecasted sun exposure information to the public at risk of UV exposure. The online system is a pre-trained EJH-X-DNN model that can integrate the new unlabeled datasets as inputs to forecast hourly ahead *UVI*. This early warning UV exposure tool can deliver the predictions in terms of low, moderate and high *UVI*, together with the evaluated aptitudes that present the predictive correctness in terms of *r*, *MAE*, *RMSE* and *LME* on the user interface. The user interface can also offer local and global model-agnostic explanations to increase the reliability and trustworthiness of model predictions. Through the offline framework, the proposed model can be continuously trained, fine-tuned and updated with the newly labeled datasets derived from the databases. The updated model via the offline framework can replace the pre-trained online model on a periodic basis to maintain robust and credible forecasting performance. Through further analysis of the user interface outputs, an expert end-user (preferably a UV specialist or a forecaster) can provide real-time sun-protection behavior recommendations to the general public to mitigate UV-exposure-related eye and skin diseases, including skin cancers.

Most of the powerful AI-inspired technologies suffer from the fact that it becomes difficult to explain why a certain outcome was predicted. The robustness of the "black-box" models is affected by even the smallest perturbations in the input data that induce dramatic effects
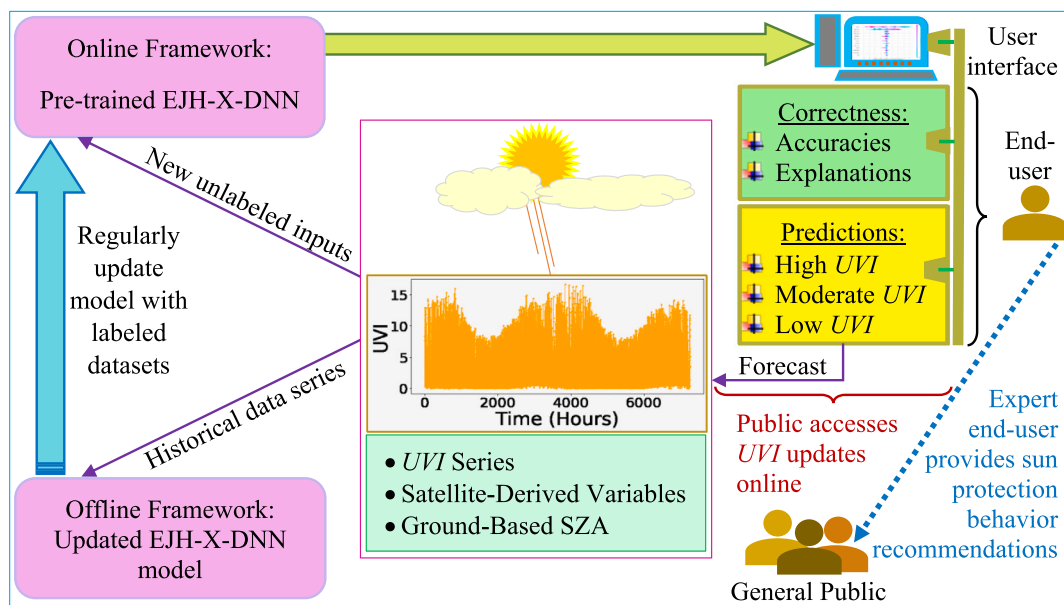
**Fig. 10.** Flowchart with real-life application of the online and offline hybrid explainable EJH-X-DNN framework in generating short-term UVI forecasts.

on the output and lead to completely different results. This is relevant in virtually all critical domains that are constrained by poor data quality due to a lack of expected independent and identically distributed (i.i.d.) datasets [70,71]. These limitations also affect the sensitive medical domain where AI-based predictive models suffer from low data quality. Consequently, the demand for trustworthy medical AI capable of explaining the "black-box" model outcomes has escalated considerably. In this regard, the regulatory requirements for AI applications in the medical domain that impacts human life have now made it mandatory to provide model explainability through traceability, transparency and interpretability capabilities [70]. On the same notion, it is imperative to include the ethical and legal aspects in the context of future trustworthy medical AI, so that all future AI-derived solutions are ethically responsible and legally compliant [71]. Explainability and robustness can promote reliability and confidence in results and enable human experts to remain in control. It ensures that human intelligence is complemented by artificial intelligence. For this purpose, the current study integrated remarkable xAI tools that enable the predictions of the newly designed DL "black-box" model to become more interpretable and trustworthy.

Though the newly constructed EJH-X-DNN model with satellite-derived predictors, ground-based SZA and lagged memory of *UVI* delivers promising forecasting capability and model explanations, future research can further boost its performance by incorporating real-time sky images as features that depict the stochastic cloud movements. Using the sky images, the temporal intermittent cloud cover effects can be extracted by integrating the merits of convolutional neural networks (CNNs) in some future research. Moreover, this research is contextualized primarily on short-term forecasting to successfully capture and predict the sudden escalated spikes of UV radiation. These spikes are led by partial cloud cover conditions that do not obscure the sun and can cause more severe skin damage with high risks of malignant keratinocyte cancer. If an investigation in the context of long-term forecasting is deemed important, future research could consider re-training the EJH-X-DNN model on long-term datasets.

## 6. Conclusions

Erythemally-effective UV radiation poses harmful exposure risks that can cause severe skin diseases such as malignant keratinocyte cancers and eye health ailments in humans. The engineering solutions pro-

vided by this study, in respect to developing an expert system that can deliver an accurate, reliable and trustworthy sun protection behaviour recommendations could be classified as an effective way to mitigate UV-exposure-related risks and provide benefits for the general public.

To address this serious issue, a hybrid explainable EJH-X-DNN model was constructed to forecast hourly ahead *UVI* for the four Australian hotspots that included Darwin, Alice Springs, Townsville and Emerald. The model was successfully trained and tested on satellite-derived and ground-based disparate datasets of the four sites. Through robust evaluation metrics and visual infographics, it was found that the prescribed model outperformed all the six benchmarked models in forecasting hourly *UVI*. The objective model displayed superior predictive performance for all four hotspots by capturing high values of $r$ and *LME* with lower error values (i.e. *MAE* and *RMSE*). Through dual-phase feature selection and hyperparameter optimization by BO, the prediction capability of the newly designed *UVI* forecasting system was further enhanced. The model-agnostic LIME tool successfully offered instance-based local interpretations, while the SHAP and PFI frameworks were highly effective in delivering global explainability of *UVI* forecasts. In accordance with the combined interpretable outcomes of the local and global model-agnostic approaches, PACF1 (i.e. antecedent lagged memory of *UVI* at a lag of $t$ - 1) and solar zenith angle were found to be the major contributing predictor variables in forecasting short-term *UVI* for all four sites. It was also found that the feature attributes associated with ozone effects, cloud cover conditions and precipitation showed some significant impact on model predictions.

The newly designed hybrid explainable EJH-X-DNN model in this research can aid the end-users in decision-making to provide more accurate, transparent and credible *UVI* exposure risk information to the general public. The performance superiority and trustworthiness of this intelligent framework can potentially extend its practical utility as an early warning tool for UV exposure through an online or mobile mode for most temperate countries. This may also be advantageous for users situated in remote locations outside the range of the current ARPANSA network.

## CRediT authorship contribution statement

**Salvin S. Prasad:** Conceptualization, Data curation, Formal analysis, Investigation, Methodology, Project administration, Resources, Software, Validation, Visualization, Writing – original draft, Writing – re-

view & editing. **Ravinesh C. Deo:** Project administration, Resources, Supervision, Writing – review & editing. **Sancho Salcedo-Sanz:** Resources, Writing – review & editing. **Nathan J. Downs:** Project administration, Resources, Supervision, Writing – review & editing. **David Casillas-Pérez:** Writing – review & editing. **Alfio V. Parisi:** Supervision, Writing – review & editing.

## Declaration of competing interest

The authors declare that they have no known competing financial interests or personal relationships that could have appeared to influence the work reported in this paper.

## Acknowledgement

## Appendix A. List of acronyms (Table A.1)

**Table A.1**
List of acronyms.

| Acronym | Definition |
| --- | --- |
| AB | AdaBoost |
| AI | Artificial Intelligence |
| ANN | Artificial Neural Network |
| ARPANSA | Australian Radiation Protection and Nuclear Safety Agency |
| AUD | Australian Dollars |
| BO | Bayesian Optimizer |
| CNN | Convolution Neural Network |
| DL | Deep Learning |
| DNN | Deep Neural Network |
| DT | Decision Tree |
| ELU | Exponential Linear Unit |
| FCN | Fully Convolutional Network |
| FFBPN | Feed-Forward Back Propagation Network |
| GIOVANNI | Goddard Online Interactive Visualization and Analysis Infrastructure |
| GPU | Graphical Processing Unit |
| ICNIRP | International Commission on Non-Ionizing Radiation Protection |
| LIME | Local Interpretable Model-Agnostic Explanations |
| LME | Legate-Mccabe Efficiency Index |
| LSTM | Long Short-Term Memory |
| MAE | Mean Absolute Error |
| MERRA | Modern-Era Retrospective Analysis for Research and Applications |
| ML | Machine Learning |
| MLP | Multilayer Perceptrons |
| NT | Northern Territory |
| PACF | Partial Autocorrelation Function |
| PFI | Permutation Feature Importance |
| QLD | Queensland |
| r | Correlation |
| $r$ | Pearson's Correlation Coefficient |
| $r_{cross}$ | Cross-Correlation Coefficient |
| ReLU | Rectified Linear Unit |
| RF | Random Forest |
| RMSE | Root Mean Squared Error |
| SGD | Stochastic Gradient Descent |
| SHAP | Shapley Additive Explanations |
| SZA | Solar Zenith Angle |
| TPU | Tensor Processing Unit |
| UNEP | United Nations Environment Programme |
| UV | Solar Ultraviolet |
| UVI | Ultraviolet Index |
| WHO | World Health Organization |
| WMO | World Meteorological Organization |
| xAI | Explainable Artificial Intelligence |

## References

[1] A. Juzeniene, J. Moan, Beneficial effects of UV radiation other than via vitamin D production, Dermato-Endocrinol. 4 (2) (2012) 109–117.

[2] W. Hijnen, E. Beerendonk, G.J. Medema, Inactivation credit of UV radiation for viruses, bacteria and protozoan (oo)cysts in water: a review, Water Res. 40 (1) (2006) 3–22.

[3] C.S. Heilingloh, U.W. Aufderhorst, L. Schipper, U. Dittmer, O. Witzke, D. Yang, X. Zheng, K. Sutter, M. Trilling, M. Alt, et al., Susceptibility of SARS-CoV-2 to UV irradiation, Am. J. Infect. Control 48 (10) (2020) 1273–1275.

[4] E. Piri, M. Babaeian, A. Tavassoli, Y. Esmaeilian, et al., Effects of UV irradiation on plants, Afr. J. Microbiol. Res. 5 (14) (2011) 1710–1716.

[5] R.C. Deo, N. Downs, A.V. Parisi, J.F. Adamowski, J.M. Quilty, Very short-term reactive forecasting of the solar ultraviolet index using an extreme learning machine integrated with the solar zenith angle, Environ. Res. 155 (2017) 141–166.

[6] A. Kazantzidis, A. Smedley, R. Kift, J. Rimmer, J.L. Berry, L.E. Rhodes, A.R. Webb, A modeling approach to determine how much UV radiation is available across the UK and Ireland for health risk and benefit studies, Photochem. Photobiol. Sci. 14 (6) (2015) 1073–1081.

[7] J. Turner, D. Igoe, A.V. Parisi, A.J. McGonigle, A. Amar, L. Wainwright, A review on the ability of smartphones to detect ultraviolet (UV) radiation and their potential to be used in UV research and for public education purposes, Sci. Total Environ. 706 (2020) 135873.

[8] E.R. Parker, The influence of climate change on skin cancer incidence–a review of the evidence, Int J. Women's Dermatol. 7 (1) (2021) 17–27.

[9] L.G. Gordon, W. Leung, R. Johns, B. McNoe, D. Lindsay, K.M. Merollini, T.M. Elliott, R.E. Neale, C.M. Olsen, N. Pandeya, et al., Estimated healthcare costs of melanoma and keratinocyte skin cancers in Australia and aotearoa New Zealand in 2021, Int. J. Environ. Res. Public Health 19 (6) (2022) 3178.

[10] L. Gordon, S. Shih, C. Watts, D. Goldsbury, A. Green, The economics of skin cancer prevention with implications for Australia and New Zealand: where are we now?, Public Health Res. Pract. 32 (1) (2022).

[11] W.H. Organization, I.C. on Non-Ionizing Radiation Protection, et al., Global solar UV index: a practical guide, Tech. Rep., World Health Organization, 2002.

[12] G.H. Bernhard, R.E. Neale, P.W. Barnes, P. Neale, R.G. Zepp, S.R. Wilson, A.L. Andrady, A.F. Bais, R.L. McKenzie, P.J. Aucamp, et al., Environmental effects of stratospheric ozone depletion, UV radiation and interactions with climate change: UNEP environmental effects assessment panel, update 2019, Photochem. Photobiol. Sci. 19 (5) (2020) 542–584.

[13] H. Majidifard, Y. Adu-Gyamfi, W.G. Buttlar, Deep machine learning approach to develop a new asphalt pavement condition index, Constr. Build. Mater. 247 (2020) 118513.

[14] A.M. Ahmed, M.H. Ahmed, S.K. Saha, O. Ahmed, A. Sutradhar, Optimization algorithms as training approach with hybrid deep learning methods to develop an ultraviolet index forecasting model, Stoch. Environ. Res. Risk Assess. 36 (10) (2022) 3011–3039.

[15] S.S. Prasad, R.C. Deo, N. Downs, D. Igoe, A.V. Parisi, J. Soar, Cloud affected solar UV prediction with three-phase wavelet hybrid convolutional long short-term memory network multi-step forecast system, IEEE Access 10 (2022) 24704–24720.

[16] G. Vilone, L. Longo, Notions of explainability and evaluation approaches for explainable artificial intelligence, Inf. Fusion 76 (2021) 89–106.

[17] L.P. Joseph, E.A. Joseph, R. Prasad, Explainable diabetes classification using hybrid Bayesian-optimized tabnet architecture, Comput. Biol. Med. 151 (2022) 106178.

[18] M. Zdravković, I. Ćirić, M. Ignjatović, Explainable heat demand forecasting for the novel control strategies of district heating systems, Annu. Rev. Control (2022).

[19] R. Qin, L.K. Mahal, D. Bojar, Deep learning explains the biology of branched glycans from single-cell sequencing data, iScience 25 (10) (2022) 105163.

[20] M. Allaart, M. van Weele, P. Fortuin, H. Kelder, An empirical model to predict the UV-index based on solar zenith angles and total ozone, Meteorol. Appl. 11 (1) (2004) 59–65.

[21] F. Orte, E. Wolfram, J. Salvador, R. D'Elia, J. Quiroga, E. Quel, A. Mizuno, Attenuation by clouds of UV radiation for low stratospheric ozone conditions, in: AIP Conference Proceedings, vol. 1810, AIP Publishing LLC, 2017, p. 110009.

[22] U. Feister, G. Meyer, U. Kirst, Solar UV radiation exposure of seamen–measurements, calibration and model calculations of erythemal irradiance along ship routes, in: AIP Conference Proceedings, vol. 1531, American Institute of Physics, 2013, pp. 860–863.

[23] S. Ghimire, B. Bhandari, D. Casillas-Perez, R.C. Deo, S. Salcedo-Sanz, Hybrid deep CNN-SVR algorithm for solar radiation prediction problems in Queensland, Australia, Eng. Appl. Artif. Intell. 112 (2022) 104860.

[24] J.N. Latosińska, M. Latosińska, J. Bielak, Towards modelling ultraviolet index in global scale. Artificial neural networks approach, Aerosp. Sci. Technol. 41 (2015) 189–198.

[25] N.K. Chauhan, K. Singh, A review on conventional machine learning vs deep learning, in: 2018 International Conference on Computing, Power and Communication Technologies (GUCON), IEEE, 2018, pp. 347–352.

[26] F. Barboza, H. Kimura, E. Altman, Machine learning models and bankruptcy prediction, Expert Syst. Appl. 83 (2017) 405–417.

[27] P. Oliveira, B. Fernandes, C. Analide, P. Novais, Multi-step ultraviolet index forecasting using long short-term memory networks, in: Distributed Computing and Artificial Intelligence, 17th International Conference, Springer, 2021, pp. 187–197.

[28] M. Chaibi, E. Benghoulam, L. Tarik, M. Berrada, A.E. Hmaidi, An interpretable machine learning model for daily global solar radiation prediction, Energies 14 (21) (2021) 7367.

[29] T. Sim, S. Choi, Y. Kim, S.H. Youn, D.-J. Jang, S. Lee, C.-J. Chun, eXplainable AI (XAI)-based input variable selection methodology for forecasting energy consumption, Electronics 11 (18) (2022) 2947.

[30] R. Saleem, B. Yuan, F. Kurugollu, A. Anjum, L. Liu, Explaining deep neural networks: a survey on the global interpretation methods, Neurocomputing (2022).

[31] S.S. Amiri, S. Mottahedi, E.R. Lee, S. Hoque, Peeking inside the black-box: explainable machine learning applied to household transportation energy consumption, Comput. Environ. Urban Syst. 88 (2021) 101647.

[32] M.S. Islam, M.A. Awal, J.N. Laboni, F.T. Pinki, S. Karmokar, K.M. Mumenin, S. Al-Ahmadi, M.A. Rahman, M.S. Hossain, S. Mirjalili, HGSORF: Henry gas solubility optimization-based random forest for C-section prediction and XAI-based cause analysis, Comput. Biol. Med. 147 (2022) 105671.

[33] R. Machlev, L. Heistrene, M. Perl, K. Levy, J. Belikov, S. Mannor, Y. Levron, Explainable artificial intelligence (XAI) techniques for energy and power systems: review, challenges and opportunities, Energy and AI (2022) 100169.

[34] C. Chen, H. Jiang, Y. Zhang, Y. Wang, Investigating spatial and temporal characteristics of harmful algal bloom areas in the East China Sea using a fast and flexible method, in: 2010 18th International Conference on Geoinformatics, IEEE, 2010, pp. 1–4.

[35] G. Huang, X. Li, C. Huang, S. Liu, Y. Ma, H. Chen, Representativeness errors of point-scale ground-based solar radiation measurements in the validation of remote sensing products, Remote Sens. Environ. 181 (2016) 198–206.

[36] N. Downs, H. Butler, A. Parisi, Solar ultraviolet attenuation during the Australian (red dawn) dust event of 23 September 2009, Bull. Am. Meteorol. Soc. 97 (11) (2016) 2039–2050.

[37] F. Ochieng'Odhiambo, Comparative study of various methods of handling missing data, Math. Model. Appl. 5 (2) (2020) 87–93.

[38] J. Yang, X. Zou, W. Zhang, H. Han, Microblog sentiment analysis via embedding social contexts into an attentive LSTM, Eng. Appl. Artif. Intell. 97 (2021) 104048.

[39] F. Pedregosa, G. Varoquaux, A. Gramfort, V. Michel, B. Thirion, O. Grisel, M. Blondel, P. Prettenhofer, R. Weiss, V. Dubourg, et al., Scikit-learn: machine learning in python, J. Mach. Learn. Res. 12 (2011) 2825–2830.

[40] N. Ketkar, N. Ketkar, Introduction to keras, in: Deep Learning with Python: A Hands-on Introduction, 2017, pp. 97–111.

[41] M. Abadi, P. Barham, J. Chen, Z. Chen, A. Davis, J. Dean, M. Devin, S. Ghemawat, G. Irving, M. Isard, et al., Tensorflow: a system for large-scale machine learning, in: OSDI, Savannah, GA, USA, vol. 16, 2016, pp. 265–283.

[42] T.M. Inc., Matlab version: 9.13.0 (r2022b), https://www.mathworks.com, 2022.

[43] H. Dai, H.-G. Hwang, V.S. Tseng, Convolutional neural network based automatic screening tool for cardiovascular diseases using different intervals of ECG signals, Comput. Methods Programs Biomed. 203 (2021) 106035.

[44] M. Alebooyeh, R.J. Urbanic, Neural network model for identifying workspace, forward and inverse kinematics of the 7-DOF YuMi 14000 ABB collaborative robot, IFAC-PapersOnLine 52 (10) (2019) 176–181.

[45] S. Ghimire, R.C. Deo, N. Raj, J. Mi, Deep learning neural networks trained with modis satellite-derived predictors for long-term global solar radiation prediction, Energies 12 (12) (2019) 2407.

[46] O. Martinez, C. Martinez, C.A. Parra, S. Rugeles, D.R. Suarez, Machine learning for surgical time prediction, Comput. Methods Programs Biomed. 208 (2021) 106220.

[47] S. Hashem, M. ElHefnawi, S. Habashy, M. El-Adawy, G. Esmat, W. Elakel, A.O. Abdelazziz, M.M. Nabeel, A.H. Abdelmaksoud, T.M. Elbaz, et al., Machine learning prediction models for diagnosing hepatocellular carcinoma with HCV-related chronic liver disease, Comput. Methods Programs Biomed. 196 (2020) 105551.

[48] X. Luo, L.O. Oyedele, A.O. Ajayi, O.O. Akinade, H.A. Owolabi, A. Ahmed, Feature extraction and genetic algorithm enhanced adaptive deep neural network for energy consumption and prediction in buildings, Renew. Sustain. Energy Rev. 131 (2020) 109980.

[49] A.T. Keleko, B. Kamsu-Foguem, R.H. Ngouna, A. Tongne, Health condition monitoring of a complex hydraulic system using Deep Neural Network and DeepSHAP explainable XAI, Adv. Eng. Softw. 175 (2023) 103339.

[50] S. Phithakkitnukooon, K. Patanukhom, M.G. Demissie, Predicting spatiotemporal demand of dockless e-scooter sharing services with a masked fully convolutional network, ISPRS Int.l J. Geo-Inf. 10 (11) (2021) 773.

[51] H.-H. Rau, C.-Y. Hsu, Y.-A. Lin, S. Atique, A. Fuad, L.-M. Wei, M.-H. Hsu, Development of a web-based liver cancer prediction model for type II diabetes patients by using an artificial neural network, Comput. Methods Programs Biomed. 125 (2016) 58–65.

[52] N. Shukla, M. Hagenbuchner, K.T. Win, J. Yang, Breast cancer data analysis for survivability studies and prediction, Comput. Methods Programs Biomed. 155 (2018) 199–208.

[53] L. Xiao, Y. Dong, Y. Dong, An improved combination approach based on adaboost algorithm for wind speed time series forecasting, Energy Convers. Manag. 160 (2018) 273–288.

[54] A.B. Nassif, Short term power demand prediction using stochastic gradient boosting, in: 2016 5th International Conference on Electronic Devices, Systems and Applications (ICEDSA), IEEE, 2016, pp. 1–4.

[55] M.M. Ghiasi, S. Zendehboudi, A.A. Mohsenipour, Decision tree-based diagnosis of coronary artery disease: cart model, Comput. Methods Programs Biomed. 192 (2020) 105400.

[56] S. Shin, Y. Lee, M. Kim, J. Park, S. Lee, K. Min, Deep neural network model with Bayesian hyperparameter optimization for prediction of nox at transient conditions in a diesel engine, Eng. Appl. Artif. Intell. 94 (2020) 103761.

[57] B. Shahriari, K. Swersky, Z. Wang, R.P. Adams, N. De Freitas, Taking the human out of the loop: a review of Bayesian optimization, Proc. IEEE 104 (1) (2015) 148–175.

[58] H.-P. Nguyen, J. Liu, E. Zio, A long-term prediction approach based on long short-term memory neural networks with automatic parameter optimization by Tree-structured Parzen Estimator and applied to time-series data of NPP steam generators, Appl. Soft Comput. 89 (2020) 106116.

[59] R. Martinez-Cantin, Bayesian optimization with adaptive kernels for robot control, in: 2017 IEEE International Conference on Robotics and Automation (ICRA), IEEE, 2017, pp. 3350–3356.

[60] M. Injadat, F. Salo, A.B. Nassif, A. Essex, A. Shami, Bayesian optimization with machine learning algorithms towards anomaly detection, in: 2018 IEEE Global Communications Conference (GLOBECOM), IEEE, 2018, pp. 1–6.

[61] E. Sharma, R.C. Deo, J. Soar, R. Prasad, A.V. Parisi, N. Raj, Novel hybrid deep learning model for satellite based PM10 forecasting in the most polluted Australian hotspots, Atmos. Environ. 279 (2022) 119111.

[62] M.T. Ribeiro, S. Singh, C. Guestrin, "Why should I trust you?" explaining the predictions of any classifier, in: Proceedings of the 22nd ACM SIGKDD International Conference on Knowledge Discovery and Data Mining, 2016, pp. 1135–1144.

[63] A. Agarwal, A. Bhatia, A. Malhi, P. Kaler, H.S. Pannu, et al., Machine learning based explainable financial forecasting, in: 2022 4th International Conference on Computer Communication and the Internet (ICCCI), IEEE, 2022, pp. 34–38.

[64] M. Kuzlu, U. Cali, V. Sharma, Ö. Güler, Gaining insight into solar photovoltaic power generation forecasting utilizing explainable artificial intelligence tools, IEEE Access 8 (2020) 187814–187823.

[65] A.E. Roth, The Shapley Value: Essays in Honor of Lloyd S. Shapley, Cambridge University Press, 1988.

[66] Z. Li, Extracting spatial effects from machine learning model using local interpretation method: an example of SHAP and XGBoost, Comput. Environ. Urban Syst. 96 (2022) 101845.

[67] Z. Jiang, L. Bo, Z. Xu, Y. Song, J. Wang, P. Wen, X. Wan, T. Yang, X. Deng, J. Bian, An explainable machine learning algorithm for risk factor analysis of in-hospital mortality in sepsis survivors with ICU readmission, Comput. Methods Programs Biomed. 204 (2021) 106040.

[68] R. Taghizadeh-Mehrjardi, N. Hamzehpour, M. Hassanzadeh, B. Heung, M.G. Goydaragh, K. Schmidt, T. Scholten, Enhancing the accuracy of machine learning models using the super learner technique in digital soil mapping, Geoderma 399 (2021) 115108.

[69] R.O. Alabi, A. Almangush, M. Elmusrati, I. Leivo, A.A. Mäkitie, An interpretable machine learning prognostic system for risk stratification in oropharyngeal cancer, Int. J. Med. Inform. 168 (2022) 104896.

[70] A. Holzinger, The next frontier: AI we can really trust, in: Joint European Conference on Machine Learning and Knowledge Discovery in Databases, Springer, 2021, pp. 427–440.

[71] A. Holzinger, M. Dehmer, F. Emmert-Streib, R. Cucchiara, I. Augenstein, J. Del Ser, W. Samek, I. Jurisica, N. Díaz-Rodríguez, Information fusion as an integrative cross-cutting enabler to achieve robust, explainable, and trustworthy medical artificial intelligence, Inf. Fusion 79 (2022) 263–278.